

Closely spaced co-rotating helical vortices: General solutions

A. Castillo-Castellanos and S. Le Dizès

*Aix Marseille Université, CNRS, Centrale Marseille, IRPHE, Marseille, France**

E. Durán Venegas

Aix Marseille Université, CNRS, Centrale Marseille, IRPHE, Marseille, France and
Departamento de Bioingeniería e Ingeniería Aeroespacial, Universidad Carlos III de Madrid, Spain*

(Dated: April 29, 2021)

In this work, we present general solutions for closely spaced co-rotating helical vortices using a filament approach. For these vortex structures, helical symmetry is broken, but solutions maintain a form of spatial periodicity. We show there exists a moving frame where vortex elements move along the structure without distorting it. These solutions can be used to characterize the evolution of the twin-tip vortices produced in the wake of a tip-splitting rotor blade. The resulting wake has a dual nature. Locally, the structure behaves much like an helical pair aligned with the locally tangent flow. However, as we move away from the vortex structure the induced flow is reminiscent of an ‘equivalent’ helical vortex with thicker core.

I. INTRODUCTION

Rotating blades, such as those of a helicopter rotor or a horizontal-axis wind turbine, generate concentrated vortices at their tips, transported downstream, creating a persistent helical pattern. These concentrated vortices can have a core size as small as 1% of the rotor radius [1]. The structure and stability of these helical vortices are associated with several practical issues actively investigated today. One of these issues concerns the interaction between a tip-vortex and a downstream surface (Vortex-Surface Interactions), which causes significant noise and vibration problems. In particular, the interaction between a tip-vortex and a rotor blade (Blade-Vortex Interaction, BVI) is responsible for reduced power output and premature structural component fatigue in wind turbines [2, 3], and undesirable noise in helicopter rotors during low speed and descending flight [4]. BVI mitigation methods can be classified as active and passive [5–7]. Active methods include dynamical modifications of the wake, for instance, by steering the wake towards a particular direction [8, 9], or by introducing a periodic perturbation [10–12]. Passive methods use a modified blade geometry to enhance particular flow features, for instance, by introducing serrations on the leading edge [13, 14] or through the use of winglets [15, 16] and slotted tips [17]. One alternative proposed by Brocklehurst and Pike [18] is to use a modified airfoil to split the tip vortex into two closely spaced vortices. As the tip vortices are advected downstream, they interact with each other and eventually merge back into a large more diffuse vortex [19]. This approach offers significant noise reduction and has no adverse effects on control load or performance [20–23], but little is known about the wake structure and the mechanism leading to a larger vortex. One of our motivations is to provide information on the vortical wake that could exist before the merging process. We consider an ideal framework of vortex filaments to illustrate the type of structures that can be created by the interaction of two closely spaced but distinct helical vortices.

A wide array of models, including analytical, experimental, and numerical approaches for rotor wake aerodynamics are available [24]. Direct numerical simulations, which require solving the Navier-Stokes equations for all scales of fluid motion up to the Kolmogorov scale remain prohibitively expensive for realistic configurations. These numerical simulations require a turbulence model, such as the Reynolds-averaged Navier-Stokes (RANS) or large eddy simulation (LES), to take into account the effect of the unresolved small scales [24–27]. These simulations may take into account the rotor directly, by solving the boundary layer along the rotor blade, or indirectly, by representing the rotor blades as body forces as in the actuator line method (ACL). For applications, the design and optimization of rotors often rely on computationally inexpensive models that describe the aerodynamic loads and wake dynamics. In the wind turbine community, blade loading is usually obtained using the Blade Element Momentum (BEM) theory, which is based on the actuator disc principle, corresponding to an infinitesimally thin rotor with an infinite number of blades. This approach has been progressively extended to include a finite number of blades, three-dimensional effects, unsteady flow loading [28], and blade thickness [29]. But using BEM requires a wake model and airfoil data [28, 30, 31]. Wakes with a prescribed helical symmetry are often used [32, 33]. Such wakes do not account for the inboard motion

* andres-alonso.castillo-castellanos@univ-amu.fr

and subsequent radial contraction (resp. expansion) observed in helicopter flight (resp. wind turbine) regimes. Additionally, a prescribed helical wake simply cannot describe the tip-vortex interaction considered here.

A free vortex method is more adequate to describe the structure and dynamics of the wake (see for instance [34]). Although the inboard motion associated with vortex formation is not easily described, the free-vortex method captures the contraction/expansion of the wake. This method has been used to extend the analytical solution of a single infinite helix [35, 36] to multiple vortices [37] and semi-infinite configurations [38, 39]. Using Joukowski's wake model, for which there is only one free tip-vortex per blade, Durán Venegas *et al.* [39] were able to find steady solutions describing the wake in all the vertical flight regimes of a helicopter (hover, climb, descent) and all wind turbine regimes, including cases for which the vortex structure is strongly deformed in the near wake and crosses the rotor plane.

For Joukowski's model, the solution matches in the far-field a uniform helix solution. When two (or more) free vortices are emitted by each blade, the solution becomes more complex even in the far-field. As shown by [37] for two counter-rotating vortices, steady solutions can still be obtained. These solutions are no longer uniform but still exhibit a spatial periodicity property. In the present work, we shall use the method developed in [37, 39] to describe the wake of tip-splitting rotors.

As for counter-rotating vortices, we expect contraction/expansion of the wake close to the rotor as well as a complex far-field. The closest canonical example to these closely spaced co-rotating helical vortex pairs is a pair of equistrength parallel vortices. In such a case, the parameters driving the vortex dynamics are the circulation Γ , separation distance d , and vortex core size a . In general, a grows with time due to viscous diffusion of vorticity with $a(t) = \sqrt{4\nu t + a_0^2}$ where ν is the kinematic viscosity, while d remains virtually constant. Simultaneously, the vortex pair rotates around the total vortex centroid with a constant rotation rate $\omega = \Gamma/(\pi d^2)$ [40]. When the ratio a/d exceeds a threshold value around 0.23, d suddenly decreases and the vortices merge into a single entity (see, for instance [41–45]). In the present work, we neglect viscous diffusion and consider a sufficiently small value of a/d , typically 0.1 such that the vortices remain distinct and the filament approach justified. We shall see that the rotation motion of the two vortices around each other is also present in our solutions.

The paper is organized as follows. Section II briefly introduces the vortex filament framework used. Section III is concerned with the far-field. We show how steady spatially-periodic solutions are obtained from a few geometric parameters. In section IV, these solutions are then used to compute the far-field contribution for the near-field solutions obtained close to a tip-splitting rotor. We present solutions representative of both wind turbine and helicopter regimes and discuss the rotor influence on the wake structure. We also provide a simple model explaining the observed spatial variations of the parameters.

II. FRAMEWORK

Our problem is defined by three spatial scales. The radius R of the rotor, the separation distance d , and the vortex core size a . The filament approach is perfectly justified as long as the core size remains small compared to other spatial scales (separation distances, local curvature radius). Closely spaced filament vortices correspond to situations for which $a \ll d \ll R$. We use the same framework as in [37, 39]. All the vorticity is considered as being concentrated along lines which move as material lines in the fluid according to

$$\frac{d\mathbf{X}_i}{dt} = \mathbf{U}(\mathbf{X}_i) + \mathbf{U}^\infty \quad (1)$$

where \mathbf{X}_i is the position vector of the i -th vortex filament, \mathbf{U} the velocity induced by the vortices and \mathbf{U}^∞ an external velocity field. The induced velocity \mathbf{U} is given by the Biot-Savart law

$$\mathbf{U}(\mathbf{X}_i) = \sum_{j=1}^n \frac{\Gamma_j}{4\pi} \int \frac{(\mathbf{X}_j - \mathbf{X}_i) \times d\mathbf{T}_j}{|\mathbf{X}_j - \mathbf{X}_i|^2} \quad (2)$$

where the integrals cover each vortex filament defined by its circulation Γ_j , position vector \mathbf{X}_j and corresponding tangent unit vector \mathbf{T}_j . Filaments are discretised in straight segments $[\mathbf{X}_i^n, \mathbf{X}_i^{n+1}]$ in order to compute the velocity field and follow its evolution. The divergence in (2) is treated using the cut-off method with a Gaussian vorticity profile [46]: to determine the local contribution to the velocity field at \mathbf{X}_i^n from the neighboring segments $[\mathbf{X}_i^{n-1}, \mathbf{X}_i^n]$ and $[\mathbf{X}_i^n, \mathbf{X}_i^{n+1}]$, we replace the two segments by an arc of circle passing through $[\mathbf{X}_i^{n-1}, \mathbf{X}_i^n, \mathbf{X}_i^{n+1}]$ and use the cut-off formula. The discretised expressions that we shall use for the induced velocity are given in [37]. When local contributions are not taken into account, the number of segments required to obtain a good approximation of the induced velocity increases by a factor $O(2\pi\rho/a)$, where ρ is the local curvature radius [37].

Our objective is to find a vortex structure that is steady in the frame of the rotor. This condition of steadiness can be written as

$$(\mathbf{U}(\mathbf{X}_j) - \mathbf{U}^F) \times \mathbf{T}_j = 0 \quad (3)$$

where \mathbf{U}^F is the frame velocity, which simply indicates that vortices are moving along the vortex structure. In practice, we shall write the steadiness condition as a system of ordinary equations. In a cylindrical frame, it can be written for each vortex as

$$\frac{dr_j}{d\zeta} = U_r(\mathbf{X}_j), \quad \frac{d\theta_j}{d\zeta} = \Omega(\mathbf{X}_j) - \Omega^F, \quad \frac{dz_j}{d\zeta} = U_z(\mathbf{X}_j) - U_z^F, \quad (4)$$

where $(r_j(\zeta), \theta_j(\zeta), z_j(\zeta))$ are the radial, angular, and axial coordinates of the j -th vortex, $(U_r, r_j\Omega, U_z)$ the corresponding velocity components, while Ω^F and U_z^F are the angular and axial velocity of the rotor frame. Each vortex curve is parametrized by ζ . These systems are to be solved with boundary conditions on the rotor, at $\zeta = 0$, where the position of each vortex is prescribed, and far-field boundary conditions at $\zeta \rightarrow \infty$.

These last boundary conditions are not trivial as the far-field is a priori unknown. Therefore, our first task is to characterize the far-field.

III. FAR-FIELD SOLUTIONS

We are interested in steady solutions created by the emission of two closely-spaced co-rotating vortices from a rotating blade tip under an external axial flow. Based on the observation of the tip vortices [47], one may naturally expect close to the rotor, a global contraction of the structure in a climbing helicopter regime, and a global expansion in a wind turbine regime. In the far-field, a quasi-uniform regime is expected. However, this regime is not as simple as for a single-tip vortex. We shall see that while not perfectly uniform, the vortices deform but exhibit a certain periodicity induced by their mutual interaction. The description of this far-field can be analyzed using the method introduced in [37] for counter-rotating vortices. These solutions are defined only by the geometrical parameters introduced in the following section.

A. Simplified approach

1. Geometrical parameters

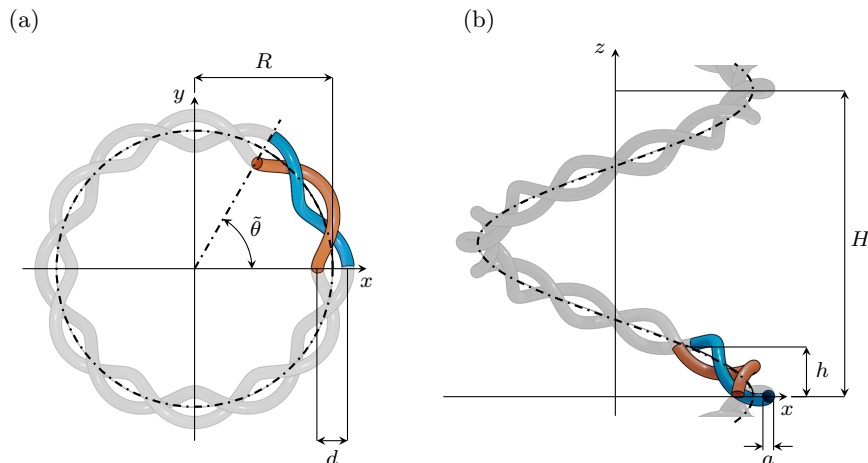


FIG. 1. Geometric parameters of closely spaced tip vortices: separation distance d , radius R , vortex core size a , axial pitches H and h , and twist parameter $\beta = \pm 2\pi/\tilde{\theta} = H/h$.

In the present situation, the far-field structure is expected to be close to a double-helix inscribed on a “larger” underlying helix. Such idealized structure is defined by the geometric parameters identified in figure 1. The double-helix has a radius $d/2$ and pitch h_τ (corresponding to an axial pitch h) while the large helix, noted \mathcal{H} , has a radius

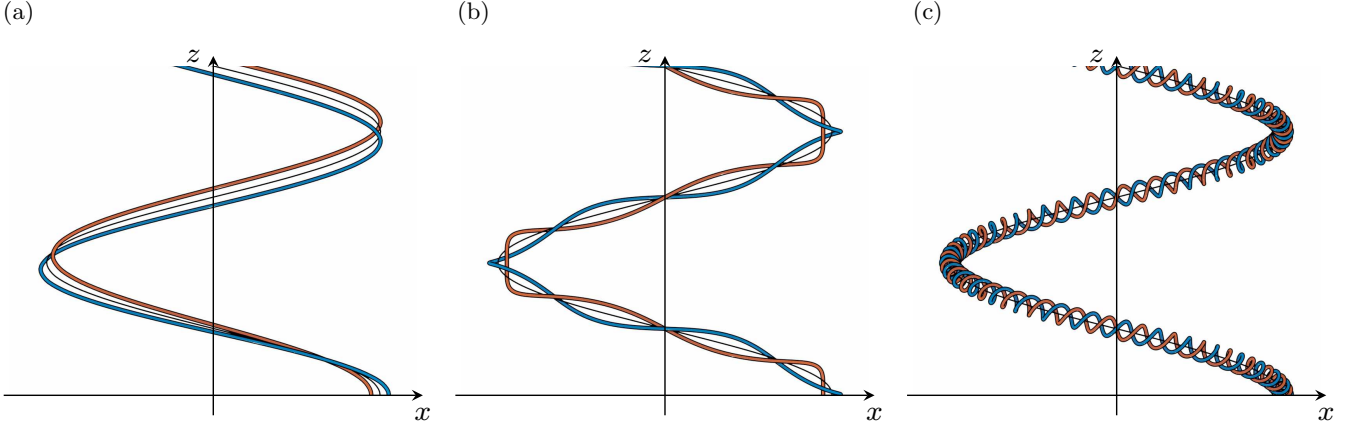


FIG. 2. Geometry described by (6) for $H = 10$, $R = 10$, $d = 1$ and: (a) $h_\tau = 128$ (or $\beta \approx 0.5$); (b) $h_\tau = 32$ (or $\beta \approx 2$); and (c) $h_\tau = 2$ (or $\beta \approx 31.8$).

R and axial pitch H . Another important parameter is the ratio $\beta \equiv H/h = 2\pi/\tilde{\theta}$ (see figure 1). Depending on the values of H , R , h_τ , and d , the double-helix structure may describe: (i) a leapfrog-type pattern, where vortices trade places every $1/\beta$ turns (figure 2a); (ii) a relatively sparse braid (figure 2b); or (iii) a dense ‘telephone cord’-type pattern (figure 2c). We are typically in situation (i) when $\beta < 1$ and $h_\tau/d > 10$, and in situation (iii) when $h_\tau/d < 5$ and $\beta > 5$.

The curve \mathbf{X}_0 described by \mathcal{H} is defined in a Cartesian frame as a function of the angular coordinate θ_0 by

$$x_0 = R \cos \theta_0 \quad (5a)$$

$$y_0 = R \sin \theta_0 \quad (5b)$$

$$z_0 = H\theta_0/(2\pi) \quad (5c)$$

while the curves $(\mathbf{X}_i, i = 1, 2)$ described by the double-helix are defined by

$$x_i = x_0 + (d/2) \cos \phi_i \cos \theta_0 - c_\tau (d/2) \sin \phi_i \sin \theta_0 \quad (6a)$$

$$y_i = y_0 + (d/2) \cos \phi_i \sin \theta_0 + c_\tau (d/2) \sin \phi_i \cos \theta_0 \quad (6b)$$

$$z_i = z_0 - c_\kappa (d/2) \sin \phi_i \quad (6c)$$

where $\phi_1 \equiv \beta\theta_0$ and $\phi_2 \equiv \beta\theta_0 + \pi$ define the orientation of the helices relative to the chord plane. The torsion coefficient c_τ and the curvature coefficient c_κ of \mathcal{H} are given by,

$$c_\tau \equiv \frac{|H|}{\sqrt{4\pi^2 R^2 + H^2}}, \quad c_\kappa \equiv \frac{2\pi R}{\sqrt{4\pi^2 R^2 + H^2}}. \quad (7)$$

We also note that h_τ and h are related with each other by the relation

$$h_\tau = \frac{h}{c_\tau}. \quad (8)$$

The above structure satisfies the following form of spatial periodicity: it is invariant by the double operation $z \rightarrow z + h$ and $\theta_0 \rightarrow \theta_0 + \tilde{\theta}$. Moreover, since we consider vortices of equal core size a and circulation Γ , both vortices are deemed as interchangeable, such that our periodic domain is further reduced to a domain of axial length $h/2$ and azimuthal angle $\tilde{\theta}/2$. In the following, we keep this property to obtain the steady solutions. In particular, we assume that there is a single location over an axial period $h/2$ where both vortices are at the same azimuth. We chose this azimuth to define the radius R and separation distance d . The axial period h then defines a mean axial pitch while H is obtained from $H = 2\pi h/\tilde{\theta}$. In addition to the core size a that is assumed constant, these length scales can be used to define four dimensionless parameters

$$R^* \equiv \frac{R}{d}, \quad H^* \equiv \frac{H}{d}, \quad h_\tau^* \equiv \frac{h_\tau}{d}, \quad \varepsilon \equiv \frac{a}{d}, \quad (9)$$

that will characterize our solutions in the far-field.

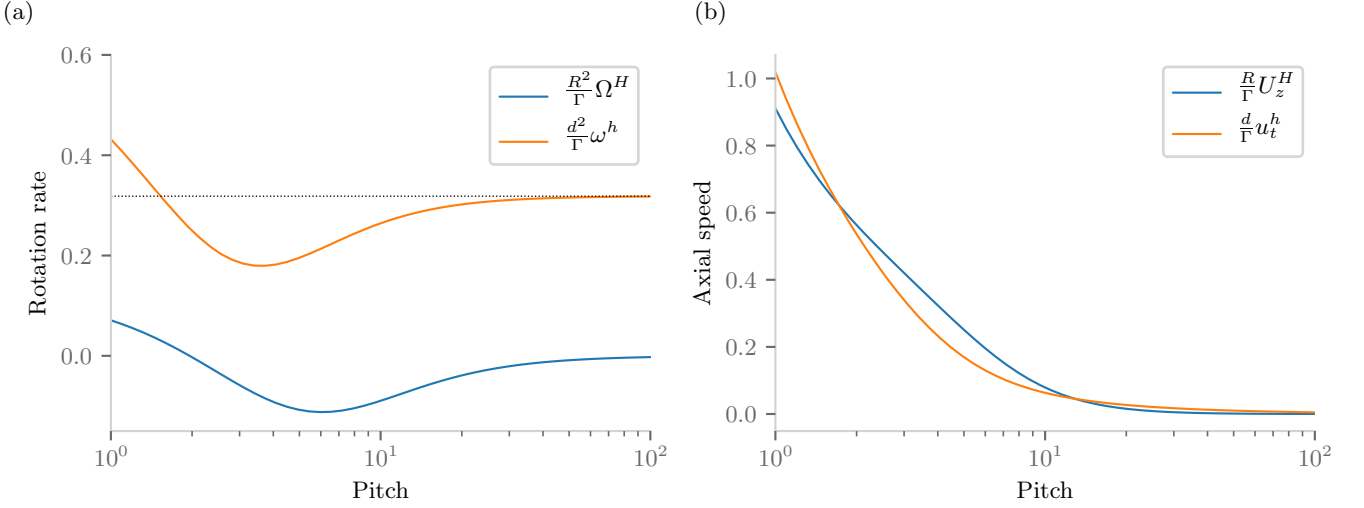


FIG. 3. Dimensionless rotation rate and axial speed of the vortex elements on a helix of radius R , circulation 2Γ and core size $d = 0.1R$ as a function of the pitch H/R (in blue), and a double-helix of radius $d/2$, circulation Γ and core size $a = 0.1d$ as a function of the pitch $2h_\tau/d$ (in orange). The dotted line in (a) indicates the value $d^2\omega^h/\Gamma = 1/\pi$ for $h_\tau \gg 1$.

2. Characteristics of the moving frame

A vortex ring and a helical vortex are examples of vortex structures that move in space at a constant speed without deformation [48]. The double-helix structure is also bound to move by the induction of velocity it generates. For this structure, one can naturally assume that the self-induced velocity is predominantly composed of:

- a translation of velocity u_t and rotation of angular velocity ω around the double-helix axis, i.e., \mathcal{H} .
- a translation of velocity U_z and rotation of angular velocity Ω around the large helix axis, i.e., the vertical axis.

Under this assumption, we can show there exists a unique frame rotating and translating along the vertical axis where the double-helix geometry shown in figure 1 remains steady. The idea is to use the property that a helix of pitch H is unperturbed by a rotation of angular velocity Ω^a and translation of axial velocity U_z^a provided that

$$U_z^a/\Omega^a = \pm H/(2\pi), \quad (10)$$

where the sign is $+$ for right-handed helices, and $-$ for left-handed helices. The self-rotation of the double-helix can then be cancelled by adding a motion of velocity $u_t^a = \mp h_\tau \omega/(2\pi)$ along the double-helix axis. This motion corresponds to an axial rotation of angular velocity $c_\kappa u_t^a/R$ plus an axial translation of velocity $c_\tau u_t^a$. These velocities add up to the self-induced velocities of the large helix. Both sums can be cancelled if one chooses the frame velocities such that

$$\Omega^F = \Omega + \frac{c_\kappa u_t}{R} \mp \frac{h}{H} \omega, \quad U_z^F = U_z + c_\tau u_t \mp \frac{c_\tau h_\tau}{2\pi} \omega. \quad (11)$$

These expressions will be used as initial guess values for the frame velocity in the numerical procedure described in the next section. If the vortices have a circulation Γ , we shall use

- for the self-induced motion (ω and u_t) of the double-helix, the values obtained by the cut-off method with a Gaussian vortex core of radius a for a straight double-helix of circulation Γ and the same geometrical parameters (pitch h_τ , radius $d/2$).
- for the self-induced motion (Ω and U_z) of the large helix \mathcal{H} , the values obtained by the cut-off method with a Gaussian vortex core of “effective” radius $d/2$ for a helix of circulation 2Γ , pitch H and radius R .

Typical values for these velocities are provided as function of the non-dimensional pitch in figure 3. In the following, we shall refer to (11) with these estimates as the rectilinear approximation for the frame velocity.

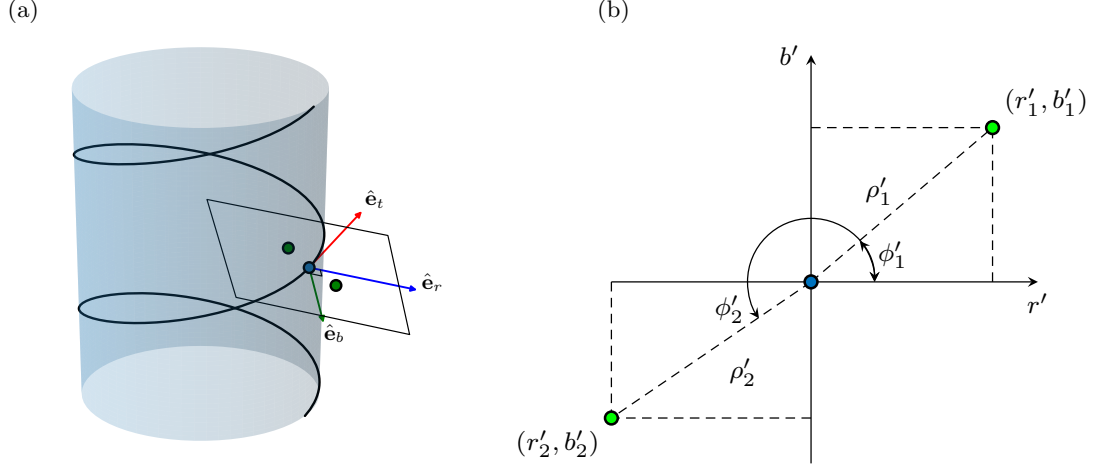


FIG. 4. (a) Local helical basis following \mathcal{H} and (b) 2-D coordinates in the (r', b') plane.

B. Numerical solutions

In the previous section, a prescribed shape for the solutions has been assumed. This hypothesis will turn out to be too strong. We shall see that the helices must deform to be compatible with the self-induced motion. For the numerical procedure, we use the separation distance d and the vortex circulation Γ to normalize time and length scales. The solutions will then only depend on the four dimensionless parameters R^* , H^* , h_τ^* and ε introduced in (9). To reduce the size of the parameter space, only H^* and h_τ^* will be varied. In most cases, we shall use $R^* = 9.5$ and $\varepsilon = 0.1$, for which the filament approach is expected to provide reliable results.

1. Governing equations in helical coordinates

To describe the far-field, it is useful to introduce a local Frenet-Serret basis $(\hat{\mathbf{e}}_{r0}, \hat{\mathbf{e}}_t, \hat{\mathbf{e}}_b)$ based on \mathcal{H} and centered at \mathbf{X}_0 as illustrated in figure 4a. The position vector \mathbf{X}_j will then be defined by its local coordinates $r'_j = (r_j - R^*)$ and b'_j in the local perpendicular basis $(\hat{\mathbf{e}}_{r0}, \hat{\mathbf{e}}_b)$, see figure 4b. Developing \mathbf{T}_j in terms of $(\hat{\mathbf{e}}_{r0}, \hat{\mathbf{e}}_t, \hat{\mathbf{e}}_b)$, the steadiness condition (3) may be written as

$$\frac{dr'_j}{d\theta_0} = \left(\frac{R^*}{c_\kappa} + c_\kappa r'_j \right) \frac{U_{r0} - U_{r0}^F}{U_t - U_t^F} + c_\tau b'_j \quad \frac{db'_j}{d\theta_0} = \left(\frac{R^*}{c_\kappa} + c_\kappa r'_j \right) \frac{U_b - U_b^F}{U_t - U_t^F} - c_\tau r'_j. \quad (12)$$

Because of the spatial periodicity and interchangeability conditions, the calculation domain is comprised between $\theta_0 = 0$ and $\theta_0 = \tilde{\theta}/2$, with

$$\tilde{\theta} = 2\pi/\beta \quad (13)$$

being the half-period of the vortex pair. Our description is completed by the following boundary conditions

$$\begin{cases} r'_1(0) = r'_2(\tilde{\theta}/2) = +\frac{1}{2}, \\ r'_2(0) = r'_1(\tilde{\theta}/2) = -\frac{1}{2}, \end{cases} \quad \begin{cases} b'_1(0) = b'_2(\tilde{\theta}/2) = 0, \\ b'_2(0) = b'_1(\tilde{\theta}/2) = 0. \end{cases} \quad (14)$$

Equation (12) is solved numerically as a non-linear minimization problem. Starting from an initial guess for (r'_j, b'_j) obtained from (6)

$$r'_1 = \frac{1}{2} \cos(\beta\theta_0), \quad b'_1 = \frac{1}{2} \sin(\beta\theta_0), \quad r'_2 = \frac{1}{2} \cos(\beta\theta_0 + \pi), \quad b'_2 = \frac{1}{2} \sin(\beta\theta_0 + \pi), \quad (15)$$

and an initial guess for Ω^F and U_z^F obtained from (11), one applies an iterative procedure. At step n of this procedure, one integrates (12) between $\theta_0 = 0$ and $\theta_0 = \tilde{\theta}/2$ to compute the new values of Ω^F and U_z^F which satisfy the boundary conditions. Then, the next iteration of (r'_j, b'_j) is computed from the residual value of (12) using Newton's method. Steps are repeated until the current and subsequent iterations converge. To fix the spatial resolution, we check for grid convergence using the primitive variables, local curvature coefficient and frame velocities. In practice, for most calculations we use $p_n = 48$ segments per period.

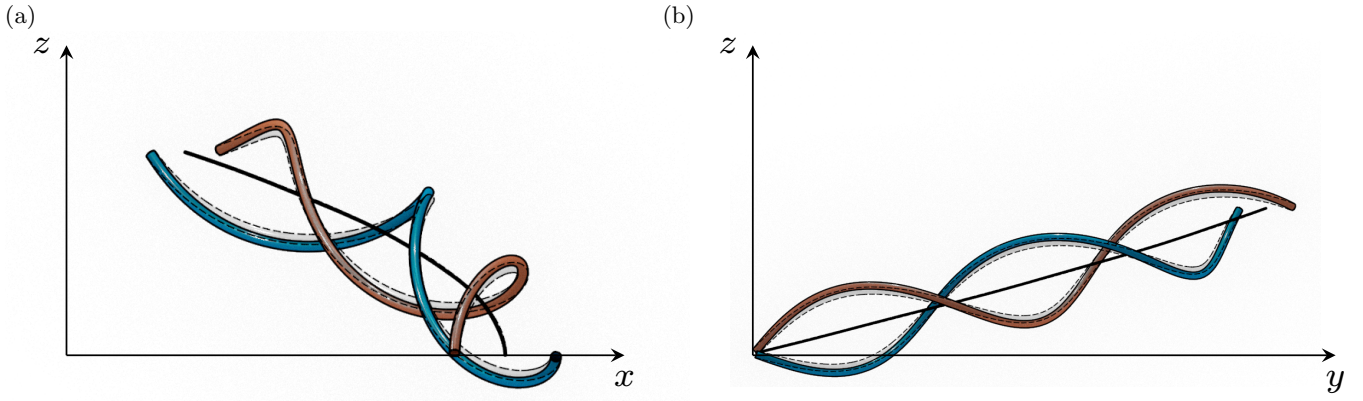


FIG. 5. Close-up of the deformed vortex structure for $H^* = 15$ and $h_\tau^* = 5$ over a single period. Numerical solution (in colour) superimposed to the undeformed initial guess (in dashed lines).

2. Geometry of the solutions

In this section, we characterize the geometry of the solutions, especially their departure from the (undeformed) initial guess. In general, solutions keep the overall form of the approximated solutions, but the helical symmetries are now broken (figure 5). Both the double-helix structure and the large underlying helix deform. Vortex segments placed in the first and second half-periods are usually drawn in opposite directions. This combined motion affects the local curvature, as it straightens vortex filaments around the nodes, and bends them around the anti-nodes. Some useful indicators of this deformation are the relative changes of the separation distance and of the mean radius defined by

$$\Delta d(\theta_0) = \sqrt{(r'_1 - r'_2)^2 + (b'_1 - b'_2)^2} - 1, \quad \Delta R(\theta_0) = \frac{\sqrt{x_1^2 + y_1^2} + \sqrt{x_2^2 + y_2^2}}{2R^*} - 1, \quad (16)$$

respectively. A positive (resp. negative) Δd indicates that the distance between the two vortices is increasing (resp. decreasing). Similarly, a positive (resp. negative) ΔR indicates an increase (resp. decrease) of the mean radius. By construction, $\Delta d(0) = \Delta d(\tilde{\theta}/2) = \Delta R(0) = \Delta R(\tilde{\theta}/2) = 0$. As seen in figure 6a-b, both quantities are shown to vary over a single period and their evolution varies with the type of solution. For leapfrogging wakes (i), Δd remains relatively constant while ΔR is positive with local maxima near $\tilde{\theta}/4$. For sparsely braided wakes (ii), Δd reaches a plateau while ΔR becomes close to zero. For densely coiled wakes (iii), ΔR may take positive and negative values, while the maximum in $\tilde{\theta}/4$ becomes a local extremum. The maximum $|\Delta d|$ and $|\Delta R|$ initially contracts, before increasing once again as H^* decreases (figure 7). Below this point, the mutually-induced velocity, which drives the rotation of the vortex pair, is no longer the dominant contribution to the total induced velocity and numerical convergence becomes increasingly hard to obtain for this family of solutions.

For applications, it is interesting to compare these solutions to a similar configuration composed of N pairs of vortices of circulation Γ . In this context, this wake geometry would represent the far-field in a Joukowski rotor wake model [49], but produced by a N -bladed tip-splitting rotor. Figure 8a (resp. 8b) displays the wake geometry obtained for two (resp. three) vortex pairs for $h_\tau^* = 2$. In general, for equal (H^*, h_τ^*) , deviations from (6) are found to increase with N (figure 7). However, if we base our comparison on the separating distance between neighbouring spires, the deformation actually decreases with N . A similar effect has been reported for counter-rotating helical vortices [39]. Finally, we note that including a straight vortex hub of circulation $-2N\Gamma$ was shown to have little effect on the wake geometry. Unless otherwise stated, in the sequel, we shall focus on the case for $N = 1$ without a hub vortex.

3. Frame and tangential velocities

The numerical procedure also provides the frame velocities Ω^F and U_z^F where the structure is steady. These quantities are plotted as a function of h_τ^* (resp. H^*) in figure 9 (resp. figure 10). They are compared to the rectilinear approximation obtained in §III A 2 (in dash-dotted lines) and to a first order approximation obtained by numerically computing the frame velocities with an undeformed solution (in dashed lines). Both approximations work well for large H^* and large h_τ^* , i.e., when self-induction is expected to be small. The first order approximation, which takes

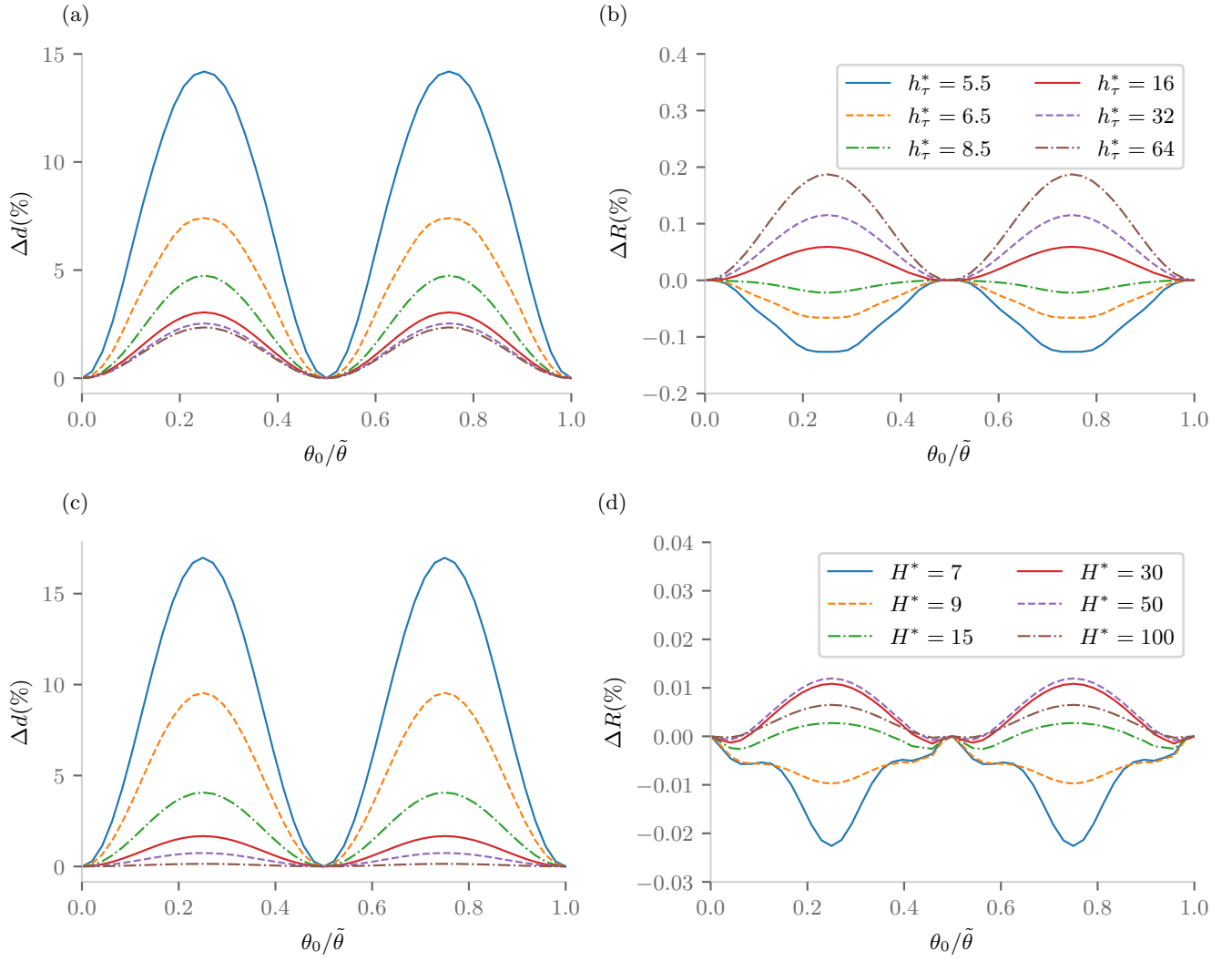


FIG. 6. (a,c) Change in the separation distance Δd and (b,d) mean radius ΔR as function of θ_0 for: (a,b) $H^* = 15$ and different h_τ^* ; and (c,d) $h_\tau^* = 10$ and different H^* .

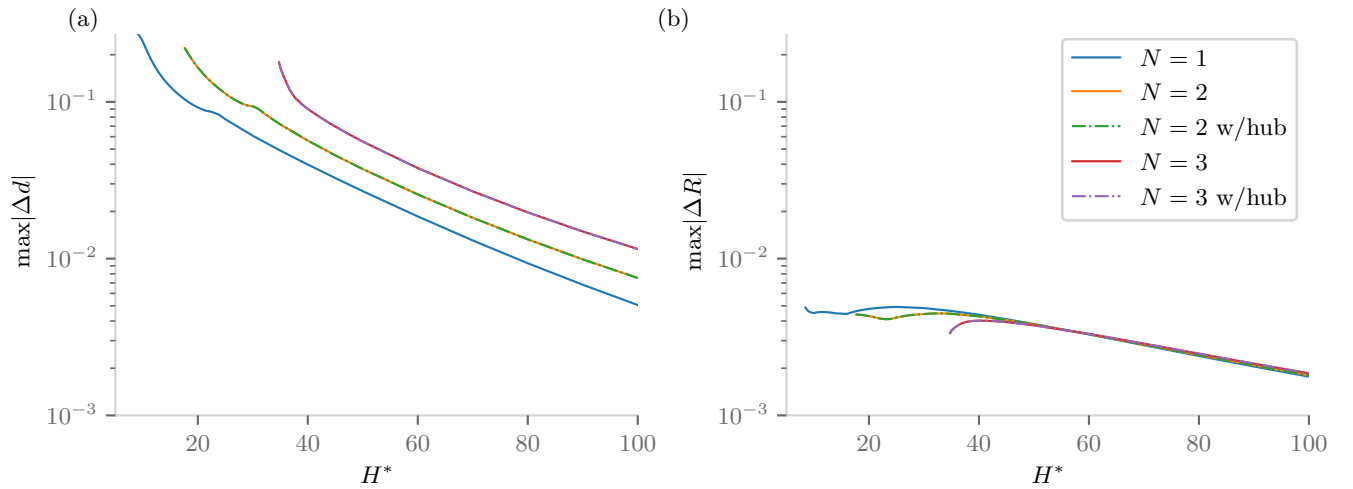


FIG. 7. Maximum change in (a) the separation distance $|\Delta d|$ and (b) mean radius $|\Delta R|$ as function of H^* for $h_\tau^* = 2$ and N vortex pairs with and without a straight hub vortex of circulation $-2N\Gamma$.

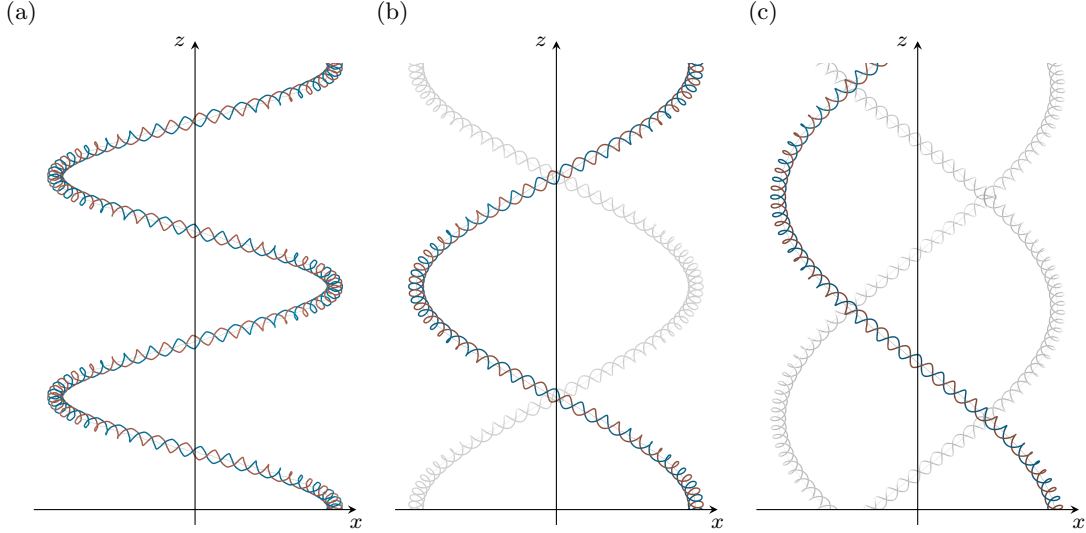


FIG. 8. Deformed structures for (a) $N = 1$, (b) $N = 2$ and (b) $N = 3$ vortex pairs for $H^*/N = 15$ and $h_\tau^* = 2$.

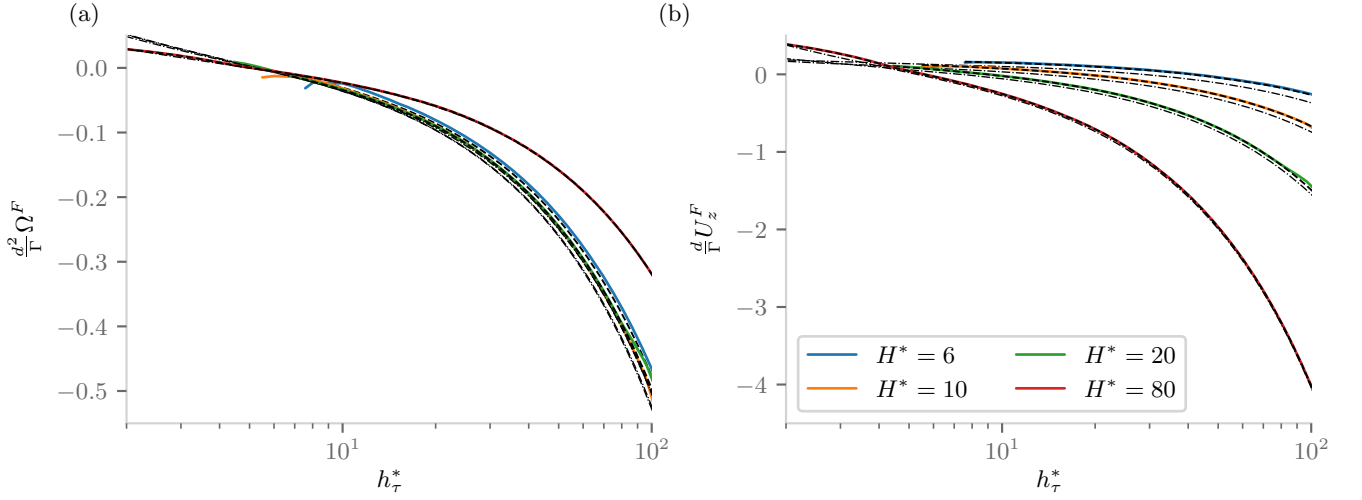


FIG. 9. Frame velocities as function of h_τ^* . Numerical solutions (in solid lines) are compared to the rectilinear approximation (in dash-dotted lines) and to a first order approximation based on the undeformed initial guess (in dashed lines).

into account the mutual- and self-induced velocities but neglects the deformation, is naturally better and provides accurate estimates whenever the deformations are weak.

Now let us consider the velocities relative to the moving frame. By construction, the vortex elements are advected along the stationary vortex structure, where positive tangential velocity U_{tan} indicates an advection in the positive axial direction and *vice versa*. In general, values of U_{tan} are positive (resp. negative) for $h_\tau^* < 0$ (resp. $h_\tau^* > 0$). The tangential velocity varies with respect to θ_0 identically for the internal and external vortices but is shifted by a half-period. Variations are generally small with respect to mean velocity \bar{U}_{tan} . As seen on figures 11a and 11b, the mean velocity displays a linear dependency on h_τ with only a weak dependency on H^* for $H^* < 10$. Figure 11a also shows that, whatever h_τ^* and H^* , the main contribution to the tangential velocity is the translation speed U_t along \mathcal{H} . We suspect that this comes from the large value of R^* that we have considered ($R^* = 9.5$).

It is also interesting to compare U_t to the velocity associated with the moving frame

$$U_t^F = c_\tau U_z^F + c_\kappa R^* \Omega^F \quad (17)$$

since the difference between the two is issued from vortex induction. For leapfrogging and weakly braided configurations ($h_\tau^* > 10$), most of the tangential velocity is associated with the moving frame and the role of vortex induction is generally small. Note in particular that when H^* is also large, we recover the estimate $\bar{U}_{tan} \approx h_\tau \Gamma / (2\pi^2 d^2)$ obtained

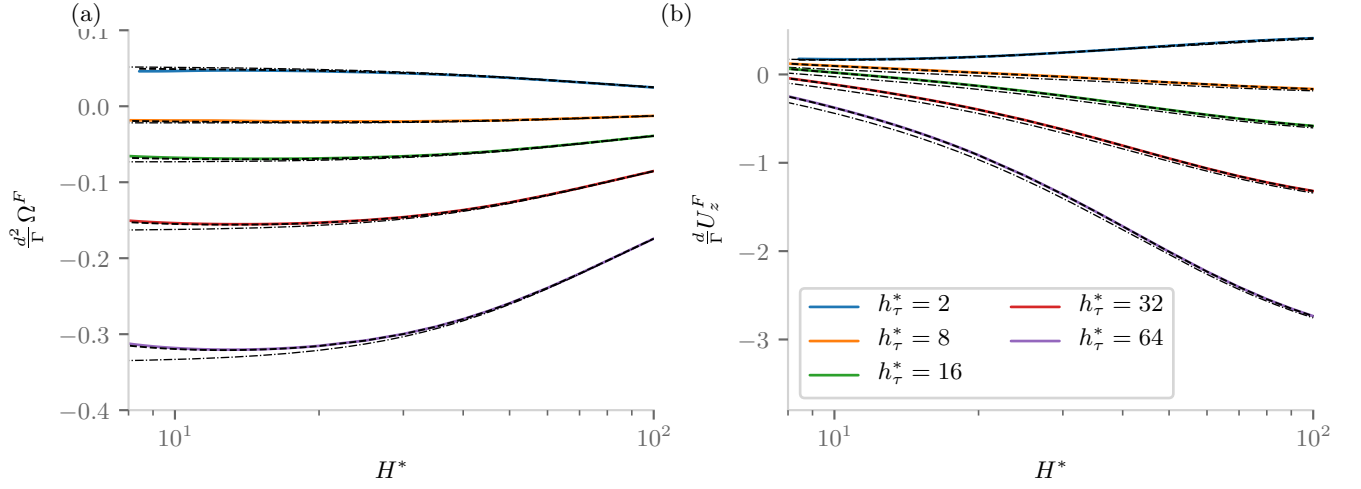


FIG. 10. Frame velocities as function of H^* . Numerical solutions (in solid lines) are compared to the rectilinear approximation (in dash-dotted lines) and to a first order approximation based on the undeformed initial guess (in dashed lines).

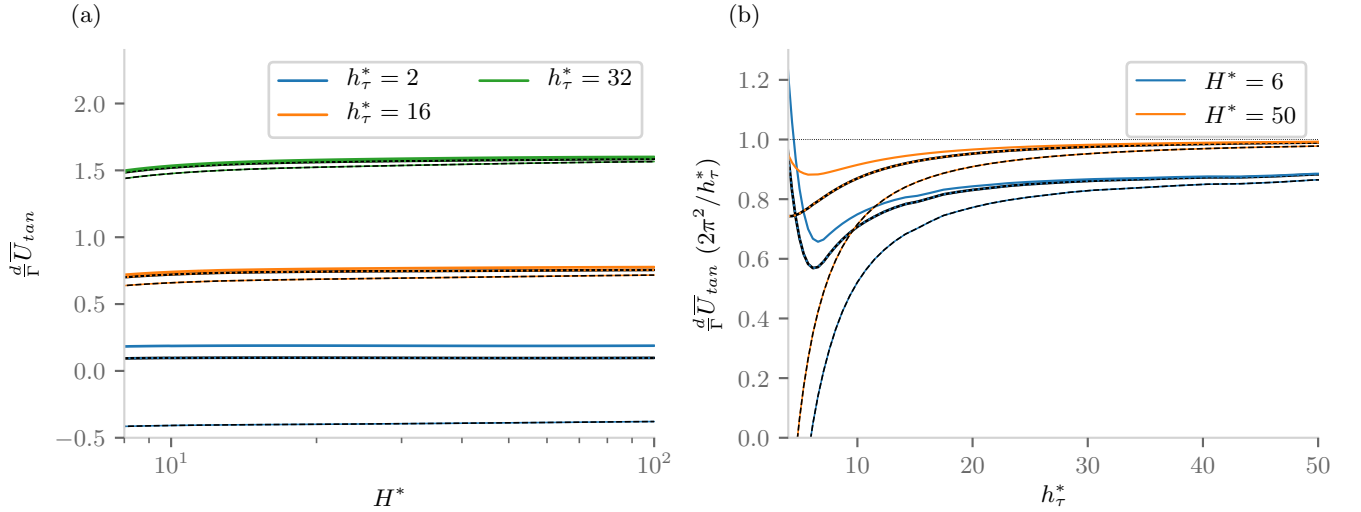


FIG. 11. Evolution of \bar{U}_{tan} (in solid lines) and \bar{U}_t (in dotted lines) as function of (a) H^* and (b) h_τ^* . Numerical solutions are also compared to the velocity associated with the moving frame \bar{U}_t^F (in dashed lines).

from the rectilinear approximation in this limit. By contrast, for densely coiled wakes, such as $h_\tau^* = 2$, \bar{U}_{tan} and \bar{U}_t can be significantly larger than the frame velocity and even point opposite directions (figure 11b).

4. Properties of the induced flow

For applications, it is useful to know the velocity field induced by the vortex structure. In this section, the induced flow is provided in cross planes and compared to the predictions obtained from the Kawada-Hardin solutions for perfect helices [35, 36, 50]. Figures 12a-c show the axial and angular velocity components taken at the plane $z = 0$ (where both vortices have the same azimuth) for a leapfrogging, sparsely braided and densely coiled structures, respectively. In these plots, we subtract the frame velocities such that the velocity field vanishes far from the center. Vortex cores intersect the plane on numerous occasions resulting in inhomogeneous velocity and vorticity distributions. For densely coiled structures, this results in regions of very intense angular velocity and opposite signed vorticity. Nevertheless, away from the cores (outside the region enclosed in dashed lines) the induced velocity is reminiscent to that of a helical vortex.

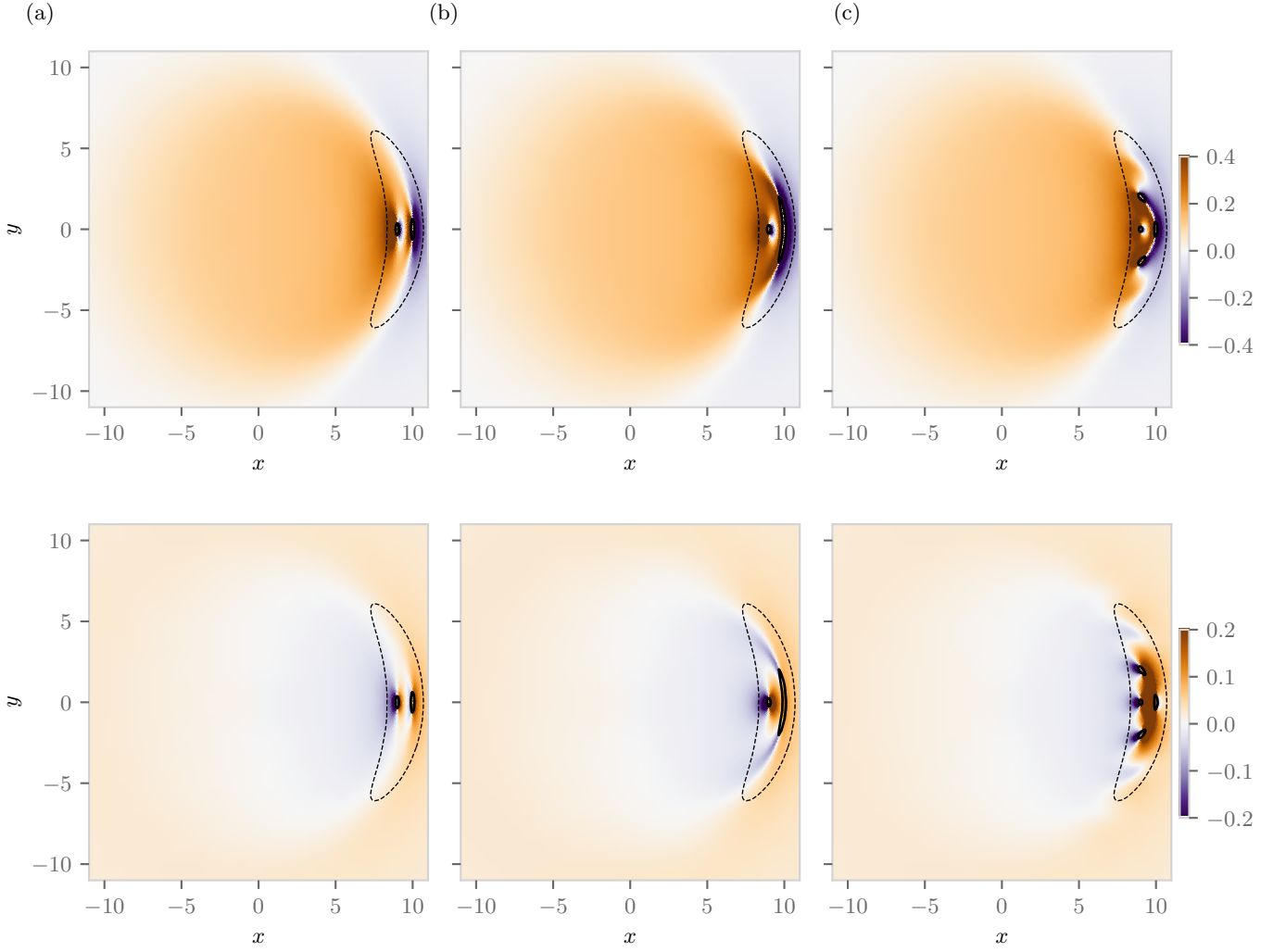


FIG. 12. Axial velocity $\frac{d}{dt}U_z$ (top) and angular velocity $\frac{d}{dt}U_\theta$ at the plane $(x, y, z) = 0$ for $H^* = 15$. (a) Leapfrogging wake for $\beta = 1$, (b) sparsely braided wake for $\beta = 4$, and (c) densely coiled wake for $\beta = 16$. Solid lines indicate the intersection with the vortex cores, while dashed lines correspond to a helical vortex tube enclosing the twin-vortex.

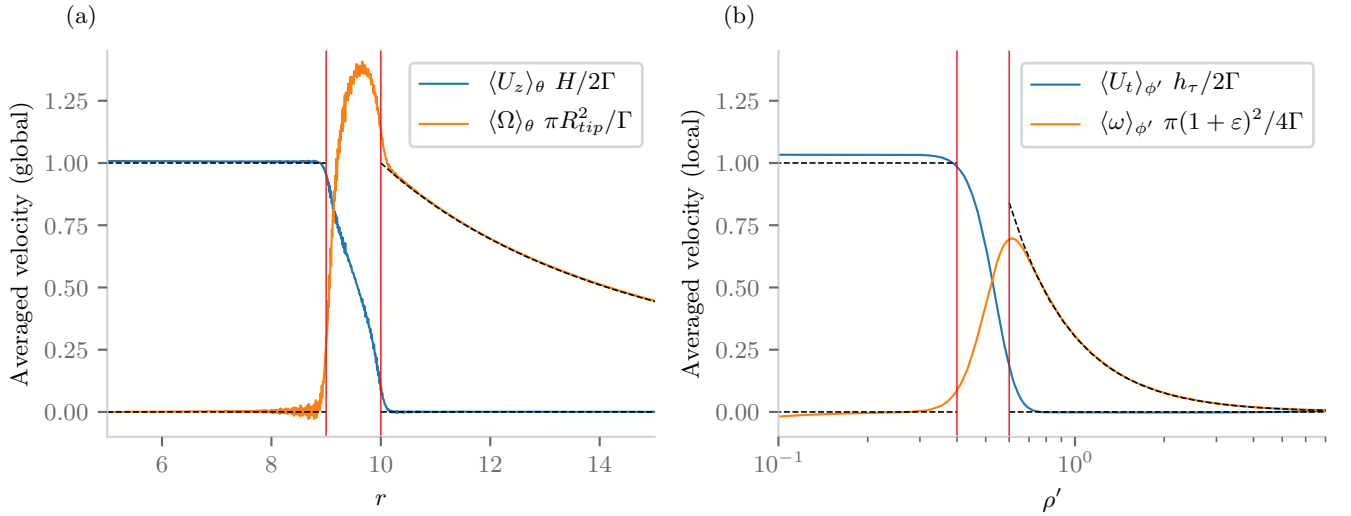


FIG. 13. Azimuthally averaged velocity profiles for $H^* = 15$ and $h_\tau^* = 2$. Fig. (a) (resp. (b)) Rotation rate and axial velocity component in the global cylindrical (resp. local helical) frame. Dashed lines correspond to expressions (18) (resp. (19)).

To highlight this similarity, consider the azimuthally averaged velocity profiles presented in figure 13a. Inside the region $R^* - \frac{1}{2} < r < R^* + \frac{1}{2}$, the angular velocity displays a maximum around $r = R^*$, while the axial velocity can be roughly approximated by a linear function. Outside the same region the azimuthally averaged profiles approach the ideal profiles of a uniform helix obtained from the Kawada-Hardin solutions [35, 36, 50]

$$\langle U_z^H \rangle_\theta = \begin{cases} 2\Gamma/H & \text{if } r < R^* - 1/2 \\ 0 & \text{if } r > R^* + 1/2 \end{cases}; \quad \langle \omega^H \rangle_\theta = \begin{cases} 0 & \text{if } r < R^* - 1/2 \\ \Gamma/(\pi r^2) & \text{if } r > R^* + 1/2 \end{cases}. \quad (18)$$

Close to the vortex cores, the velocity field can be better understood by projecting the velocity components into the local helical frame (ρ', ϕ') . This is shown in figure 13b, where the ϕ' -averaged profiles also approach the mean profiles of a perfect double-helix locally aligned with \mathcal{H}

$$\langle U_t^h \rangle_{\phi'} = \begin{cases} 2\Gamma/h_\tau & \text{if } \rho' < (1 - \varepsilon)/2 \\ 0 & \text{if } \rho' > (1 + \varepsilon)/2 \end{cases}; \quad \langle \omega^h \rangle_{\phi'} = \begin{cases} 0 & \text{if } \rho' < (1 - \varepsilon)/2 \\ \Gamma/(\pi \rho'^2) & \text{if } \rho' > (1 + \varepsilon)/2 \end{cases}. \quad (19)$$

The above results highlight the dual nature exhibited by this vortex structure. Solutions for closely spaced co-rotating helical vortices issue from a balance between contributions at different scales with long-distance effects primarily governed by the large-scale helix and more local features defined by the double-helix geometry.

IV. NEAR-FIELD SOLUTIONS

In the previous section, we have described the solutions in the far-field. In this section, we consider the vortex structure close to the rotor plane. The objective is not to perform a complete parametric study but to illustrate how these solutions can describe the wake of a tip-splitting rotor under different flight regimes.

A. Numerical method

There is one notable difference with respect to the analysis performed in the previous section. Instead of fixing the geometric parameters to find the associated frame velocities, now we solve the inverse problem. That is, we fix the operating conditions, i.e., the rotation rate $\Omega^F = \Omega_R$ and external velocity $U_z^F = -U_\infty$, and compute the corresponding wake geometry. Now the prescribed geometrical parameters are the radial coordinates $r = R_{fin} = R_0 - d_0/2$ and $r = R_{tip} = R_0 + d_0/2$ where the vortices are emitted on the rotor blade (located at $\theta_0 = 0$ and $z = 0$), and the vortex core size a . As previously, we define four non-dimensional parameters

$$\lambda \equiv \frac{R_0 \Omega_R}{U_\infty}, \quad \eta \equiv \frac{\Gamma}{R_0^2 \Omega_R}, \quad R_0^* \equiv \frac{R_0}{d_0}, \quad \varepsilon_0^* \equiv \frac{a}{d_0}, \quad (20)$$

where λ is known as the tip-speed ratio and η represents the relative vortex strength. As in [39], we choose a convention such that η remains positive, while λ may change sign. Wind turbine regimes will always correspond to positive values of λ . By contrast, helicopters may correspond to either negative values of λ in climbing flight or positive values of λ in descending flight. In the present study, only the parameters η and λ are varied. In most cases, ε_0^* and R_0^* are fixed to 0.1 and 9.5, respectively. Note that these parameters are different from the parameters R^* and ε^* defined above for the far-field, as the mean radius and the vortex separation distance in the far-field are now the results of the calculation.

The near-field solution satisfies (4) with the boundary condition at $\zeta = 0$: $r_1 = R_0^* - \frac{1}{2}$ and $r_2 = R_0^* + \frac{1}{2}$ and $\theta_j = z_j = 0$. As we go away from the rotor, it should match a far-field solution. To implement this condition, we follow the numerical procedure used by Durán Venegas *et al.* [39] for Joukowski's rotor wake model. We decompose the induced velocity into contributions from the near-field and far-field. Contributions from the far-field are modeled by imposing that after a certain distance from the rotor plane, the wake adopts the geometry of a far-field solution (see figure 14). The geometrical parameters of this far-wake solution are estimated from the near-field solution at the end of calculation domain. The computational domain must be large enough for the wake to develop and match the far-field. In practice, the size of the domain and of the corresponding far-wake range from 30π to 60π .

B. Description of the steady solutions

Figure 15 displays the wake structure with the corresponding radial coordinates as function of the axial coordinate z . Figure 15a (resp. 15b) is representative of the wind turbine (resp. helicopter) regime, which displays a radial expansion

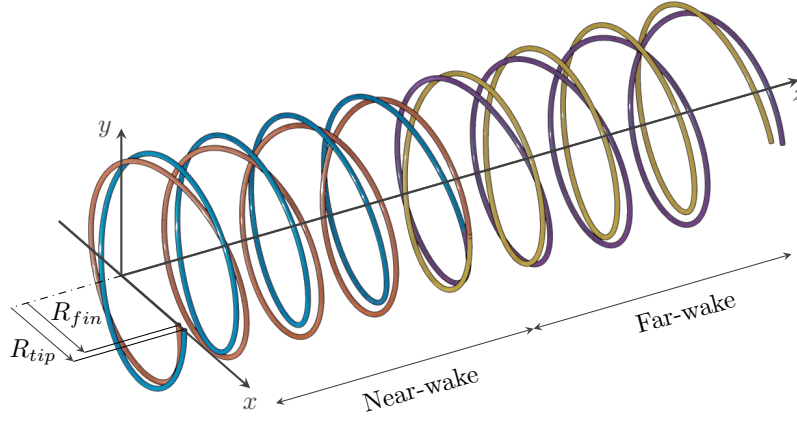


FIG. 14. Schematic representation of the semi-infinite case: two co-rotating vortices are emitted from a rotor blade at radial positions R_{fin} and R_{tip} , respectively. The calculation domain and the prescribed far-wake are shown in different colors.

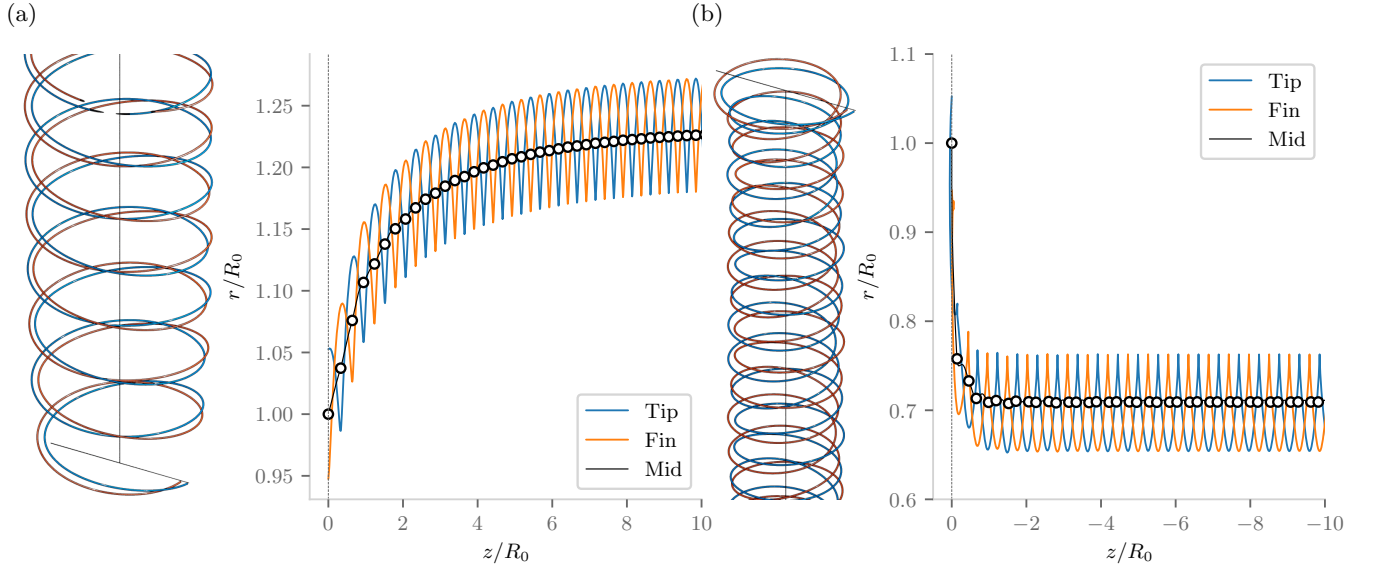


FIG. 15. Schematic representation of the vortex wake and evolution of the radial coordinates r_j as function of z for $\eta = 0.04$, $R_0^* = 9.5$, $\varepsilon_0^* = 0.1$. (a) $\lambda = 5.5$ in a wind turbine regime; (b) $\lambda = 40$ in a helicopter descending flight regime. Markers indicate the positions where both vortices have the same azimuth.

(resp. contraction), while the two vortices trade places continuously. Simultaneously, the separation distance may also contract or expand due to the combined effects of the vortex pair and the rotor's presence. Additionally, the structure may exhibit local variations of both axial pitches. For clarity, we characterize the wake in terms of the geometric parameters introduced in §III.

1. Evolution of the wake in the near-field

As in §III, we introduce the curve $\mathbf{X}_{mid}(\zeta)$ equidistant to both vortices and the separation distance $d(\zeta)$ defined by

$$\mathbf{X}_{mid}(\zeta) = (\mathbf{X}_{tip}(\zeta) + \mathbf{X}_{fin}(\zeta))/2, \quad (21)$$

$$d(\zeta) = \|\mathbf{X}_{tip}(\zeta) - \mathbf{X}_{fin}(\zeta)\|. \quad (22)$$

We also perform a series of discrete measurements at the points along the curve $(\zeta_n, n = 1, 2, \dots)$ where the internal and external vortices have the same azimuth (indicated by solid marks in figure 15). In this way, the large helix \mathcal{H}

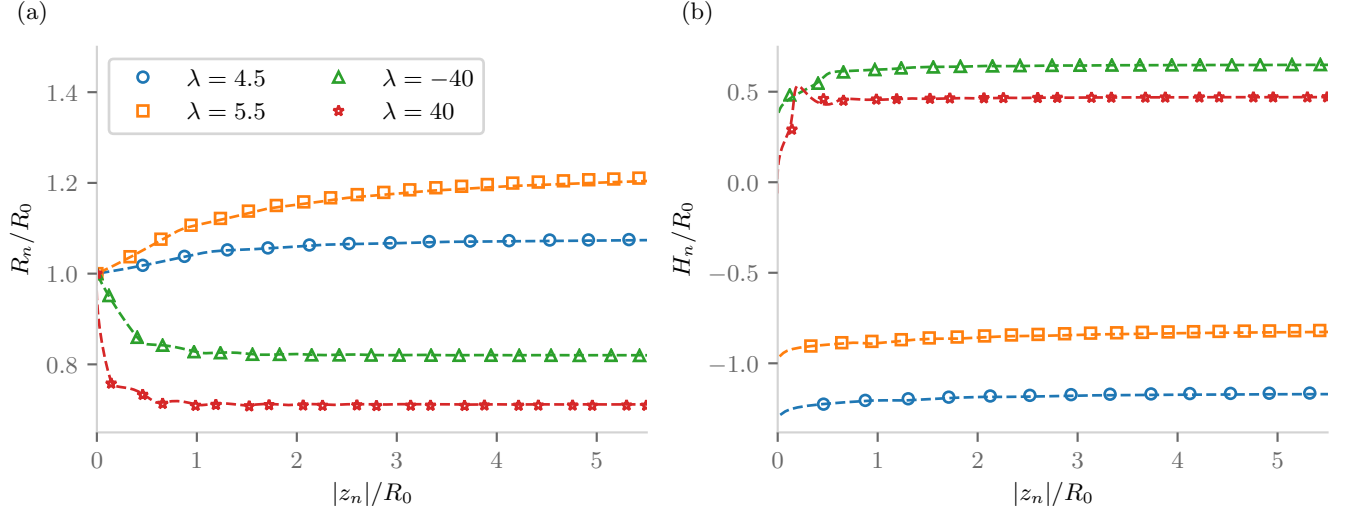


FIG. 16. Evolution of (a) R_n/R_0 , and (b) H_n/R_0 as function of $|z_n|/R_0$ for different values of λ for $\eta = 0.04$, $R_0^* = 9.5$, $\varepsilon_0^* = 0.1$. For each case, we display the corresponding evolution obtained for an ‘equivalent’ helical vortex in dashed lines.

is characterized by a set of radii and pitches

$$R_n \equiv r_{mid}(\zeta_n), \quad H_n \equiv \frac{z_{mid}(\zeta_{n+1}) - z_{mid}(\zeta_n)}{\theta_{mid}(\zeta_{n+1}) - \theta_{mid}(\zeta_n)}, \quad \text{for } n = 0, 1, 2, \dots \quad (23)$$

which converge towards the values at the far-field R_∞ and H_∞ , respectively.

Figure 16a displays the evolution of R_n/R_0 as a function of $z(\zeta_n)/R_0$ for cases representative of wind turbine and helicopter regimes. Far-field solutions suggest that \mathcal{H} can be modeled by a single tip vortex of circulation 2Γ and core size d emitted from the radial coordinate R_0 under the same operating conditions. A good agreement is observed between the evolution of R_n/R_0 and the equivalent helix approximation. A similar agreement is observed between H_n/R_0 and the ‘equivalent’ pitch in figure 16b.

Conversely, the rotation of the vortex pair is characterized by a set of mean separation distances and axial pitches

$$d_n \equiv d(\zeta_n), \quad h_n \equiv \frac{z_{mid}(\zeta_{n+1}) - z_{mid}(\zeta_n)}{\pi}, \quad \text{for } n = 0, 1, 2, \dots \quad (24)$$

which converge towards the values at the far-field d_∞ and h_∞ , respectively. Combining both sets of measurements, we obtain a set for the mean pitch and twist parameter

$$h_{\tau,n} \equiv h_n \frac{\sqrt{H_n^2 + 4\pi^2 R_n^2}}{H_n}, \quad \beta_n \equiv \frac{H_n}{h_n}, \quad \text{for } n = 1, 2, \dots \quad (25)$$

which converge towards the values at the far-field $h_{\tau,\infty}$ and β_∞ .

The evolution of these parameters is shown in figures 17a-c. The first remarkable feature is a dynamical similarity between local parameters’ evolution and those of the large helix. Variations are limited to the very near wake, and are rapid whenever those of the large helix are rapid. However, variations seem to be opposite for the small and the large helix: the separation distance d_n increases (resp. decreases) when the large helix radius R_n decreases (resp. increases). The local pitch $h_{\tau,n}$ is also found to have an opposite sign to H_n , meaning that the small and large helices are oriented differently. Additionally, both pitches remain constant in the wake. It is also important to note the large absolute value of $h_{\tau,n}/d_0$, indicating that configurations are weakly twisted where self-induced effects are generally small. This has some consequences that can be used to derive a model explaining the variations of the local properties.

The evolution of the separation distance d_n can be understood by the following arguments. As the radius R_n of the large helix varies, we expect variations of the advection speed U_t of the vortices along \mathcal{H} . These variations are responsible of a local strain that tends to contract the vortex structure (that is, decrease d) when U_t increases, and expand it when U_t decreases. The variations of d are then obtained by the conservation of the mass flux in the vortex stream tube which prescribes that

$$U_t(\zeta_n) d^2(\zeta_n) = cst. \quad (26)$$

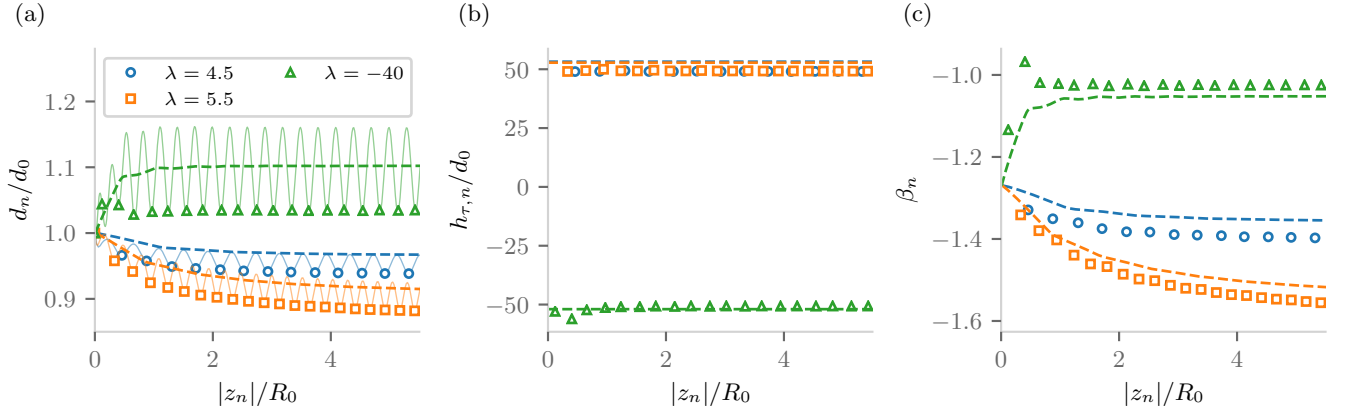


FIG. 17. Evolution of (a) d_n/d_0 , (b) $h_{\tau,n}/d_0$ and β_n as a function of z_n/R_0 for the cases displayed in figure 16. Dashed lines in figures (a) and (b), correspond to (28) and (29), respectively. For reference, the evolution of $d(z)/d_0$ is shown in solid lines in fig. (a).

An estimate for $U_t(\zeta_n)$ can be obtained when the self-induction is weak. We have seen in §III that in that case, $U_t(\zeta_n)$ is mainly provided by the frame velocity $U_t^F(\zeta_n) = \pm(U_\infty^2 + R_n^2\Omega_R^2)^{1/2}$ where the \pm sign is defined by the sign of U_∞ . In terms of the non-dimensionalized parameters λ and η , this gives

$$U_t(\zeta_n) \frac{R_0}{\Gamma} \approx \frac{\sqrt{1 + \lambda^2 R_n^2/R_0^2}}{\eta\lambda} \quad (27)$$

Combining this expression with (26), we obtain the following relation between d_n and R_n

$$\frac{d_n}{d_0} = \left[\frac{1 + \lambda^2}{1 + \lambda^2 R_n^2/R_0^2} \right]^{1/4} \quad (28)$$

This expression is tested in figure 17a, where a contraction (resp. expansion) of the separation distance is observed for the wind turbine (resp. helicopter) regimes. While equation (28) gives correct trends and orders of magnitude, it tends to overestimate the expansion and underestimate the contraction. This difference could be explained in different ways. First, the contributions from the double-helix to U_t estimated at the far-field from (19) as $2R_0^*d_0/h_{\tau,n}$ have been neglected in (27) since vortex induction is rather weak. Second, a radial contraction of the double-helix close to the blade that should also be present but that has not been taken into account. Such contraction could be estimated by analogy to a vortex pair under a locally axial flow U_t . Considering these two effects, would give an additional contraction as observed in the numerics, but still would be too small to account for the discrepancy. Another possibility is the differential expansion/contraction experienced by the two vortices close to the rotor plane due to their radial position. The outermost vortex would experience a larger expansion/contraction than the innermost vortex, thus changing the separation distance. However, since the two vortices continuously trade places with one another, this effect is hard to quantify.

In a similar vein, the pitch of the double-helix can be estimated using $h_\tau = 2\pi U_t/\omega$ where ω is the rotation rate of the vortex pair. As shown in figure 3, for large values of h_τ/d we can approximate ω as $\omega = \Gamma/\pi d^2$. Combining both expressions shows that $h_{\tau,n}$ should be constant and given by

$$\frac{h_{\tau,n}}{d_0} \approx \frac{2\pi^2}{\eta R_0^*} \left[\frac{\sqrt{1 + \lambda^2}}{\lambda} \right] \quad (29)$$

which is verified in figure 17b. Equation (29) also suggests that $h_{\tau,n}/d_0$ is primarily governed by R_0^* and η , since the part shown in brackets remains close to 1 (in absolute value). The condition $h_{\tau,n}/d_0 > 10$ for being weakly twisted then reduces to $\eta R_0^* \lesssim 2$. For $\eta = 0.04$, this condition is satisfied as soon as $R_0^* \lesssim 50$.

From (29), we can also compute the twist parameter $\beta_n = H_n/(h_{\tau,n}c_\tau(\zeta_n))$ as

$$\beta_n \approx -\frac{\eta(R_0^*)^2}{\pi} \left[\frac{|\lambda|}{\sqrt{1 + \lambda^2}} \frac{\sqrt{H_n^2 + 4\pi^2 R_n^2}}{2\pi R_0} \right]. \quad (30)$$

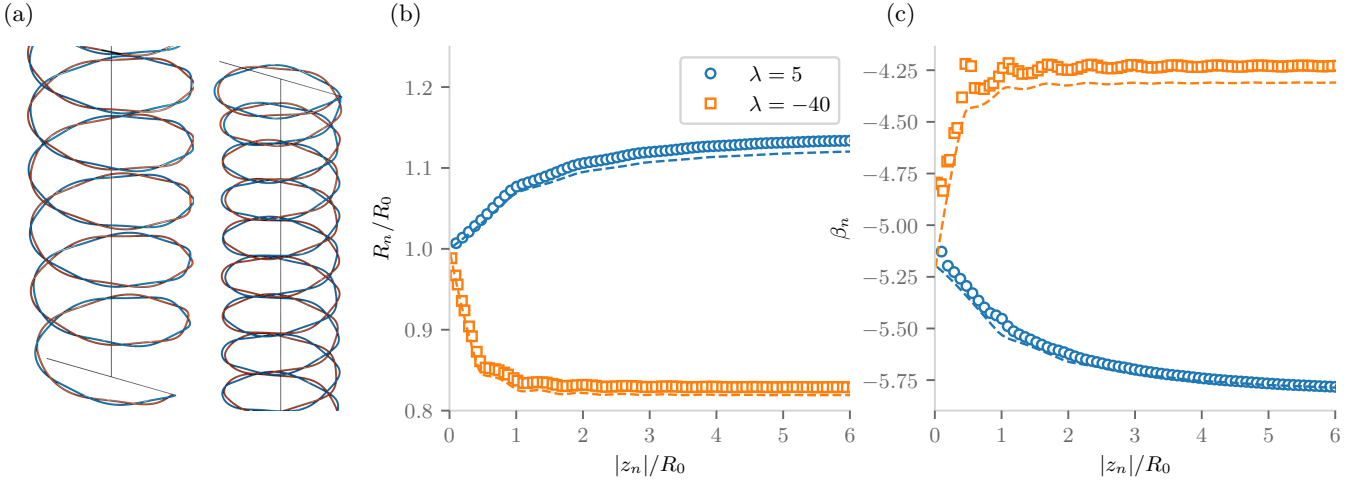


FIG. 18. (a) Sparsely braided wakes obtained for $\eta = 0.04$, $R_0^* = 19.5$, $\varepsilon_0^* = 0.1$ in a wind turbine regime ($\lambda = 5$) and a helicopter climbing flight regime ($\lambda = -40$). (b,c) Evolution of R_n/R_0 and β_n compared to the equivalent helix approximation in dashed lines.

which has been compared to the data in figure 17c. As the part shown in brackets remains in general close to 1, the typical order of $|\beta|$ is then given by the product $\eta(R_0^*)^2$. In particular, we expect to be in a leapfrogging situation, i.e. $|\beta| < 1$, as soon as $\eta(R_0^*)^2 \lesssim \pi$. Equation (30) suggests a simple way to control the twist parameter by increasing R_0^* (i.e. reducing the separation distance d_0). In order to illustrate this point, we consider the same values of (λ, η) for $R_0^* = 19.5$ in different flight regimes and measure β_n . As expected, the evolution of the large-scale pattern is comparable to the equivalent single tip rotor, while β_n is roughly four times larger with respect to the case with $R_0^* = 9.5$ (compare figure 17c and figure 18c).

The above approximations can also be used to predict the characteristics of the far-wake. In figures 19 and 20, we have compared the model with the numerics as both λ and η vary. We can observe in figures 19a,b and 20a,b that for the radius R_∞ and the pitch H_∞ , the agreement with the equivalent vortex approximation is excellent for all regimes. For the separation distance d_∞ (figures 19c and 20c), the trend is qualitatively good but there is a constant systematic over-estimation in the model, that has already been noticed above. The fact that d_∞ changes little with R_0^* is also consistent with (29). Interestingly, the twist parameter β_∞ (figures 19d and 20d) is always found to be well-predicted, probably because it does not directly depend on the separation distance.

V. CONCLUSIONS

In this article, we have provided a vortex wake model for a tip-splitting rotor in any incident normal wind, which applies to all the vertical helicopter flight and wind turbine regimes. This model is based on a simplified description of the wake with a pair of co-rotating vortex filaments attached to each blade at different radial positions. A free-vortex method together with Biot & Savart law has been used to obtain steady solutions in a frame moving with the rotor blades.

We have first analyzed the structure of the solutions in the far-field. As for counter-rotating vortices [37], we have shown that steady periodic solutions can be obtained in specific reference frames and that the properties of these solutions are governed by 4 purely geometrical dimensionless parameters (R/d , H/d , h_τ/d and a/d). We have documented the fluctuations of the separation distance and of the mean radius, as well as the variations of the frame velocities with respect to two of these parameters (H/d and h_τ/d). We have shown that these solutions can be understood in terms of two interlaced helical vortices inscribed on top of a larger helical structure, which allowed us to obtain good estimates for the wake geometry and the frame velocities.

The far-field solutions have then been used to get near-wake solutions. We have solved the semi-infinite free-vortex problem with a prescribed condition on the blade (the vortices are attached at given positions) and a condition of matching with a far-field solution away from the rotor. We have been able to obtain steady solutions in the frame rotating with the rotor, that capture the expected global expansion/contraction of the wake as well as the deformations induced by the mutual interaction of the vortices. Interestingly, we have also been able to show that the solution is well described by a small-scale twisted structure inscribed onto a large-scale pattern obtained for a single large

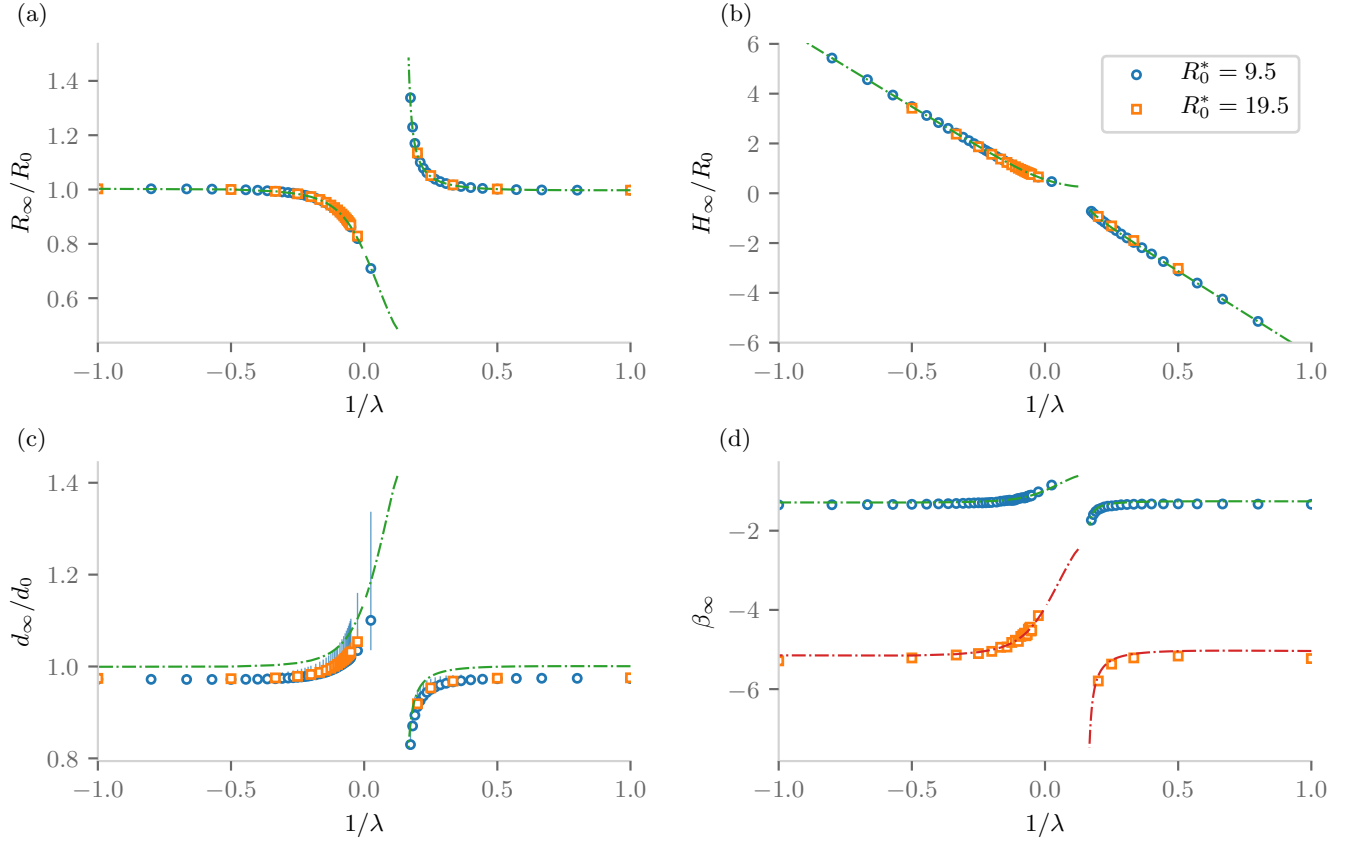


FIG. 19. Evolution of the far-wake parameters as a function of $1/\lambda$ for $\eta = 0.04$, $\varepsilon_0^* = 0.1$. Dashed lines correspond to the equivalent vortex approximations in (a,b) and to equations (29) and (30) in (c,d). For reference, fig. (c) also displays the minimum and maximum values of $d(\zeta)/d_0$ for $\zeta \rightarrow \infty$ as a vertical bar. Helicopter regimes are on the left, wind turbine regimes on the right.

tip-vortex with the total circulation. We have further shown how the variations of the parameters of the small-scale structure are driven by the large-scale motion.

In applications, the core size of tip vortices is sufficiently small to make the filament approach relevant. For instance, in the MEXICO project, a wind turbine of diameter 4.5 m creates a tip vortex of radius 2 cm giving a ratio $a/R \sim 0.01$ [51]. Similar values can be found in helicopter rotor wakes [52]. In such cases, there is clearly enough room to generate a second tip vortex at a small distance d from the tip such that a/d remains small. We therefore claim that the typical parameters $a/d = 0.1$ and $R/d = 10$ that we have considered in the present study can be obtained in real applications. However, it does not mean that our analysis will automatically apply. The roll-up process giving rise to the vortices could be significantly more complex. In a recent experimental study, Schröder *et al.* [19] succeeded in creating a second vortex close to the tip using a fin. However, the fin vortex was also found to contain negative vorticity contributions coming from the vorticity sheet shed by the modified blade, that made it unstable with respect to the centrifugal instability. In that case, the second vortex is thus rapidly disrupted and our solution cannot be formed. We suspect that if the blade was more tapered close to the tip, the fin vortex would not have been unstable and a different evolution would have been observed.

Our solutions are nevertheless expected to be unstable. Helical solutions are indeed known to be unstable with respect to a long-wavelength instability, the so-called Widnall instability [53, 54]. As shown in Quaranta *et al.* [11] and Huang *et al.* [12], this instability can be excited to accelerate the destruction of the vortices. In a follow-up paper [55], the linear stability of our solutions is analyzed using the filament framework. Owing to the higher complexity of our solutions, we demonstrate that there exist different types of instability modes. As for the Widnall instability [10, 11], each instability mode is nevertheless shown to be associated with a specific pairing event.

Short-wavelength instabilities such as the curvature instability [56] and the elliptic instability [57, 58] are also expected to develop in the core of the vortices. These instabilities cannot be described by the filament approach which neglects everything occurring in the vortex cores. It requires monitoring the core deformations induced by curvature, torsion and strain fields which are responsible for these instabilities. This can be done by matched asymptotic

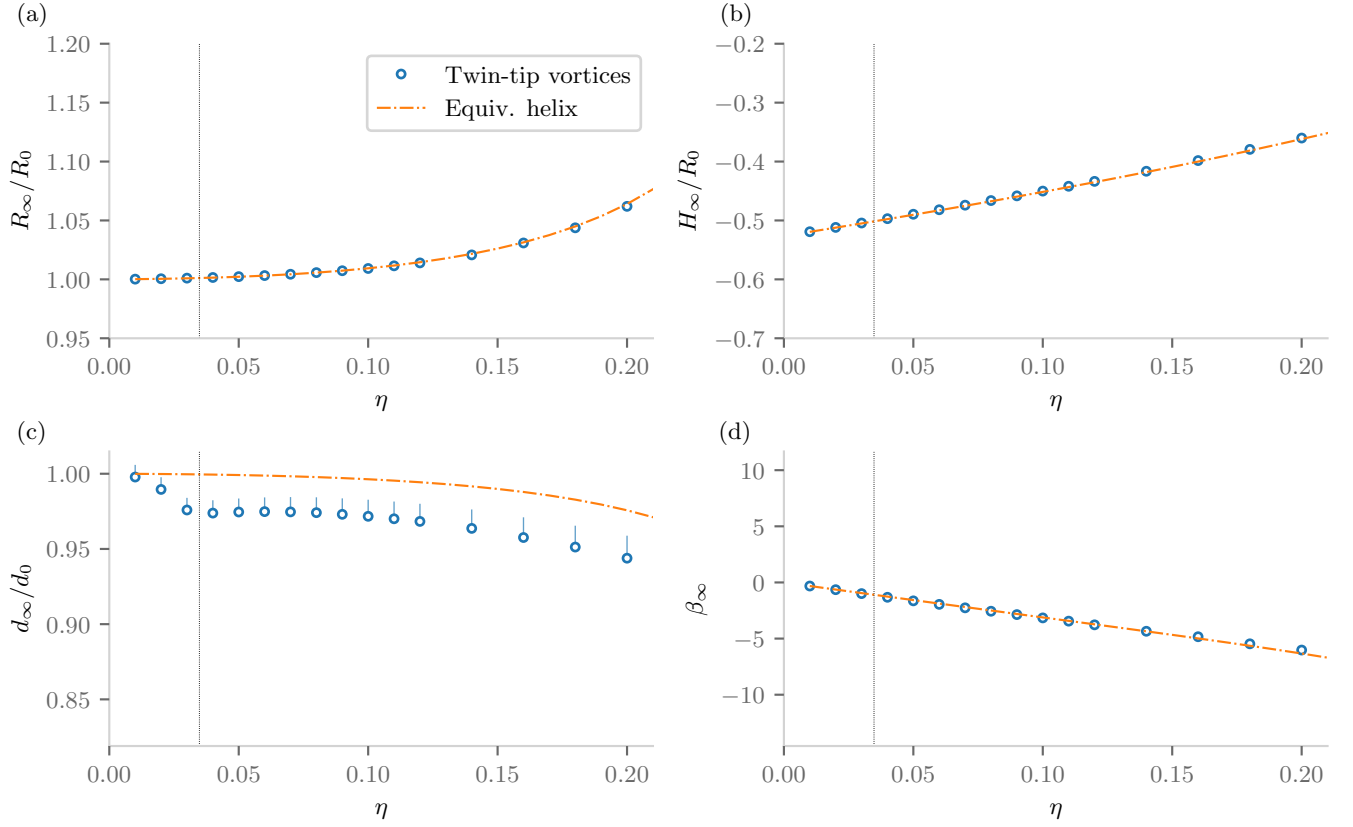


FIG. 20. Evolution of the far-wake parameters as a function of η for $\lambda = 2$ (wind turbine regime), $R_0^* = 9.5$ and $\varepsilon_0^* = 0.1$. Dashed lines correspond to the equivalent vortex approximations in (a,b) and to equations (29) and (30) in (c,d). For reference, fig. (c) also displays the minimum and maximum values of $d(\zeta)/d_0$ for $\zeta \rightarrow \infty$ as a vertical bar. The vertical dotted line in (c) indicates the value $\eta = \pi/(R_0^*)^2$ where $\beta_\infty \approx 1$.

techniques [59, 60] or by direct numerical simulations when the base flow exhibits particular symmetries as shown by [40] for 2D vortex pairs, [61] for rings and [62] for helices. The internal core structure that is obtained can then be used for the short-wavelength stability study (see for instance [61, 63]).

Note that the determination of a quasi-steady solution may not always be necessary for the stability study if the time scale of the instability is long compared to the relaxation time scale needed to get the correct core structure. Brynjell-Rahkola and Henningson [64] have indeed shown that they could obtain the correct stability properties of a helix with a Gaussian vorticity core by just analysing the temporal evolution of the numerical solution obtained from the initial condition formed by the filament structure with the prescribed axisymmetric vortex profile in the core. This is an interesting result as it provides a simple way to analyse the short-wavelength stability properties of our solutions.

ACKNOWLEDGMENT

This work is part of the French-German project TWIN-HELIX, supported by the Agence Nationale de la Recherche (grant no. ANR-17-CE06-0018) and the Deutsche Forschungsgemeinschaft (grant no. 391677260).

-
- [1] L. A. Young, Vortex core size in the rotor near-wake, NASA Technical Report TM-2003-212275 (2003).
 - [2] K. S. Hansen, R. J. Barthelmie, L. E. Jensen, and A. Sommer, The impact of turbulence intensity and atmospheric stability on power deficits due to wind turbine wakes at horns rev wind farm, *Wind Energy* **15**, 183 (2012).
 - [3] R. J. Barthelmie and L. Jensen, Evaluation of wind farm efficiency and wind turbine wakes at the nysted offshore wind farm, *Wind Energy* **13**, 573 (2010).

- [4] F. Gandhi and L. Tauszig, Influence of individual interactions on helicopter blade-vortex interaction noise, in *Proceedings of the 26th European Rotorcraft Forum* (2000).
- [5] J. C. Hardin and S. L. Lamkin, Concepts for reduction of blade/vortex interaction noise, *J. Aircr.* **24**, 120 (1987).
- [6] Y. H. Yu, Rotor blade-vortex interaction noise, *Prog. Aerosp. Sci.* **36**, 97 (2000).
- [7] A. Brocklehurst and G. Barakos, A review of helicopter rotor blade tip shapes, *Prog. Aerosp. Sci.* **56**, 35 (2013).
- [8] P. Fleming, J. Annoni, J. J. Shah, L. Wang, S. Ananthan, Z. Zhang, K. Hutchings, P. Wang, W. Chen, and L. Chen, Field test of wake steering at an offshore wind farm, *Wind Energy* **2**, 229 (2017).
- [9] F. Campagnolo, R. Weber, J. Schreiber, and C. L. Bottasso, Wind tunnel testing of wake steering with dynamic wind direction changes, *Wind Energy* **5**, 1273 (2020).
- [10] H. U. Quaranta, H. Bolnot, and T. Leweke, Long-wave instability of a helical vortex, *J. Fluid Mech.* **780**, 687 (2015).
- [11] H. U. Quaranta, M. Brynjell-Rahkola, T. Leweke, and D. S. Henningson, Local and global pairing instabilities of two interlaced helical vortices, *J. Fluid Mech.* **863**, 927 (2019).
- [12] X. Huang, S. A. Moghadam, P. Meysonnat, M. Meinke, and W. Schröder, Numerical analysis of the effect of flaps on the tip vortex of a wind turbine blade, *Int J Heat Fluid Flow* **77**, 336 (2019).
- [13] S. Ito, Aerodynamic influence of leading-edge serrations on an airfoil in a low Reynolds number, *J. Biomech. Sci. Eng.* **4**, 117 (2009).
- [14] E. Pang, A. Cambray, D. Rezgui, M. Azarpeyvand, and S. A. Showkat Ali, Investigation towards a better understanding of noise generation from UAV propellers, in *2018 AIAA/CEAS Aeroacoustics Conference* (2018) p. 3450.
- [15] J.-J. Chattot, Effects of blade tip modifications on wind turbine performance using vortex model, *Comput Fluids* **38**, 1405 (2009).
- [16] A. Ebrahimi and R. Mardani, Tip-vortex noise reduction of a wind turbine using a winglet, *J. Energy Eng.* **144**, 04017076 (2018).
- [17] Y. O. Han and J. G. Leishman, Investigation of helicopter rotor-blade-tip-vortex alleviation using a slotted tip, *AIAA journal* **42**, 524 (2004).
- [18] A. Brocklehurst and A. Pike, Reduction of BVI noise using a vane tip, in *AHS Aeromechanics Specialists Conference* (American Helicopter Society, 1994).
- [19] D. Schröder, T. Leweke, R. Hörschemeyer, and E. Stumpf, Experiments on helical vortex pairs in the wake of a rotor, in *AIAA Scitech 2021 Forum* (2021) p. 1088.
- [20] C. Copland, F. Coton, and R. M. Galbraith, An experimental study of the idealised vortex system of a novel rotor blade tip, *Aeronaut. J* **102**, 385 (1998).
- [21] F. N. Coton, R. B. Green, and R. M. Galbraith, Analysis of model rotor blade pressures during parallel interaction with twin vortices, *J. Aircr.* **42**, 1552 (2005).
- [22] C.-H. Cho, D.-J. Lee, C. Hwang, and Kari, Numerical investigations of parallel BVI noise with split tip vortices, in *AHS International 62nd Annual Forum*, Vol. I (American Helicopter Society, 2006) pp. 13 – 19.
- [23] J. Jung, W. Y. Choi, and S. Lee, Effect of the blade inner-tip position on the generation of twin vortices, *J. Aircr.* **45**, 728 (2008).
- [24] B. Sanderse, S. Van der Pijl, and B. Koren, Review of computational fluid dynamics for wind turbine wake aerodynamics, *Wind energy* **14**, 799 (2011).
- [25] R. J. Stevens and C. Meneveau, Flow structure and turbulence in wind farms, *Annual review of fluid mechanics* **49**, 311 (2017).
- [26] D.-G. Caprace, P. Chatelain, and G. Winckelmans, Wakes of rotorcraft in advancing flight: A large-eddy simulation study, *Phys. Fluids* **32**, 087107 (2020).
- [27] E. Branlard, *Wind turbine aerodynamics and vorticity-based methods*, Vol. 7 (Springer, 2020).
- [28] J. N. Sørensen, *General momentum theory for horizontal axis wind turbines*, Vol. 4 (Springer, 2016).
- [29] G. Van Kuik, J. N. Sørensen, and V. Okulov, Rotor theories by Professor Joukowski: momentum theories, *Prog. Aerosp. Sci.* **73**, 1 (2015).
- [30] W. Z. Shen, M. O. Hansen, and J. N. Sørensen, Determination of the angle of attack on rotor blades, *Wind Energy* **12**, 91 (2009).
- [31] J. N. Sørensen, Aerodynamic aspects of wind energy conversion, *Annu. Rev. Fluid Mech.* **43**, 427 (2011).
- [32] S. Goldstein, On the vortex theory of screw propellers, *Proc. R. Soc. Lond. A* **123**, 440 (1929).
- [33] V. L. Okulov and J. N. Sørensen, Optimum operating regimes for the ideal wind turbine, in *J. Phys. Conf. Ser.*, Vol. 75 (IOP Publishing, 2007) p. 012009.
- [34] J. G. Leishman, M. J. Bhagwat, and A. Bagai, Free-vortex filament methods for the analysis of helicopter rotor wakes, *J. Aircr.* **39**, 759 (2002).
- [35] S. Kawada, Induced velocity by helical vortices, *J. Aeronaut. Sci.* **3**, 86 (1936).
- [36] J. C. Hardin, The velocity field induced by a helical vortex filament, *Phys. Fluids* **25**, 1949 (1982).
- [37] E. Durán Venegas and S. Le Dizès, Generalized helical vortex pairs, *J. Fluid Mech.* **865**, 523 (2019).
- [38] W. O. Miller and D. B. Bliss, Direct periodic solutions of rotor free wake calculations, *J Am Helicopter Soc* **38**, 53 (1993).
- [39] E. Durán Venegas, P. Rieu, and S. Le Dizès, Structure and stability of Joukowski’s rotor wake model, *J. Fluid Mech.* **911**, A6 (2021).
- [40] S. Le Dizès and A. Verga, Viscous interactions of two co-rotating vortices before merging, *J. Fluid Mech.* **467**, 389 (2002).
- [41] M. Melander, N. Zabusky, and J. McWilliams, Symmetric vortex merger in two dimensions: causes and conditions, *J. Fluid Mech.* **195**, 303 (1988).

- [42] P. Meunier, U. Ehrenstein, T. Leweke, and M. Rossi, A merging criterion for two-dimensional co-rotating vortices, [Phys. Fluids](#) **14**, 2757 (2002).
- [43] C. Cerretelli and C. Williamson, The physical mechanism for vortex merging, [J. Fluid Mech.](#) **475**, 41 (2003).
- [44] C. Josserand and M. Rossi, The merging of two co-rotating vortices: a numerical study, [Eur. J. Mech. B Fluids](#) **26**, 779 (2007).
- [45] T. Leweke, S. Le Dizès, and C. H. Williamson, Dynamics and instabilities of vortex pairs, [Annu. Rev. Fluid Mech.](#) **48**, 507 (2016).
- [46] P. G. Saffman, [Vortex dynamics](#) (Cambridge university press, 1992).
- [47] J. Leishman, [Principles of Helicopter Aerodynamics](#), Cambridge Aerospace Series (Cambridge University Press, 2016).
- [48] H. Lamb, [Hydrodynamics](#), Dover Books on Physics (Dover publications, 1945).
- [49] N. E. Zhukovskii and V. P. Vetchinkin, [Théorie tourbillonnaire de l'hélice propulsive](#) (Gauthier-Villars, 1929).
- [50] Y. Fukumoto, V. L. Okulov, and D. H. Wood, The contribution of kawada to the analytical solution for the velocity induced by a helical vortex filament, [Appl. Mech. Rev.](#) **67** (2015).
- [51] H. Snel, J. Schepers, and B. Montgomerie, The MEXICO project (model experiments in controlled conditions): The database and first results of data processing and interpretation, in [J Phys Conf Ser](#), Vol. 75 (IOP Publishing, 2007) p. 012014.
- [52] A. Bauknecht, B. Ewers, O. Schneider, and M. Raffel, Blade tip vortex measurements on actively twisted rotor blades, [Exp Fluids](#) **58**, 1 (2017).
- [53] S. E. Widnall, The stability of a helical vortex filament, [J. Fluid Mech.](#) **54**, 641 (1972).
- [54] B. Gupta and R. Loewy, Theoretical analysis of the aerodynamic stability of multiple, interdigitated helical vortices, [AIAA journal](#) **12**, 1381 (1974).
- [55] A. Castillo-Castellanos, E. Durán Venegas, and S. Le Dizès, Closely spaced co-rotating helical vortices: Long-wave instability, Manuscript in preparation (2021).
- [56] F. J. Blanco-Rodríguez and S. Le Dizès, Curvature instability of a curved Batchelor vortex, [J. Fluid Mech.](#) **814**, 397 (2017).
- [57] R. R. Kerswell, Elliptical instability, [Annu. Rev. Fluid Mech.](#) **34**, 83 (2002).
- [58] F. J. Blanco-Rodríguez and S. Le Dizès, Elliptic instability of a curved Batchelor vortex, [J. Fluid Mech.](#) **804**, 224 (2016).
- [59] A. Callegari and L. Ting, Motion of a curved vortex filament with decaying vortical core and axial velocity, [SIAM J. Appl. Math](#) **35**, 148 (1978).
- [60] F. J. Blanco-Rodríguez, S. Le Dizès, C. Selçuk, I. Delbende, and M. Rossi, Internal structure of vortex rings and helical vortices, [J. Fluid Mech.](#) **785**, 219 (2015).
- [61] Y. Hattori, F. Blanco-Rodríguez, and S. Le Dizès, Numerical stability analysis of a vortex ring with swirl, [J. Fluid Mech.](#) **878**, 5 (2019).
- [62] C. Selçuk, I. Delbende, and M. Rossi, Helical vortices: linear stability analysis and nonlinear dynamics, [Fluid Dyn. Res.](#) **50**, 011411 (2017).
- [63] C. Roy, N. Schaeffer, S. Le Dizès, and M. Thompson, Stability of a pair of co-rotating vortices with axial flow, [Phys. Fluids](#) **20**, 094101 (2008).
- [64] M. Brynjell-Rahkola and D. S. Henningson, Numerical realization of helical vortices: application to vortex instability, [Theor. Comp. Fluid Dyn](#) **34**, 1 (2020).